RSC Advances

ROYAL SOCIETY OF CHEMISTRY

www.rsc.org/advances

Table of contents

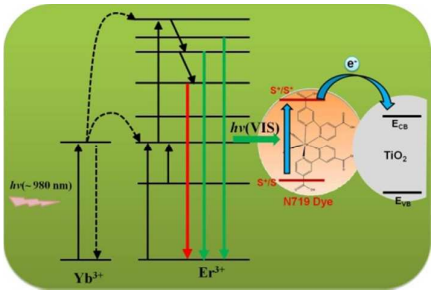

This review focuses on the various synthetic approaches for upconversion nanocrystals and recent developments on the photovoltaic applications of upconversion nanomaterials.

Cite this: DOI: 10.1039/c0xx00000x

www.rsc.org/xxxxxx

ARTICLE TYPE

Upconversion nanophosphors for solar cell applications

Parthiban Ramasamy, Palanisamy Manivasakan, and Jinkwon Kim*

Received (in XXX, XXX) Xth XXXXXXXXX 20XX, Accepted Xth XXXXXXXXX 20XX
DOI: 10.1039/b000000x

Currently, one of the major factor limiting the efficiency of solar cells is the spectral mismatch between the energy distribution of photons in the incident solar spectrum and the bandgap of a semiconductor material. To reduce the spectral mismatch losses, wavelength conversion of sunlight is regarded as an effective route. Both upconversion and downconversion materials are currently explored as spectral convertors for solar cells. In an upconversion process, photons with an energy lower than the band gap of the solar cell are converted to higher energy photons that can be absorbed by the semiconductor. This review focuses on the various synthetic approaches for upconversion nanocrystals and methods to improve the upconversion luminescence, as well as giving an overview on the recent developments on the photovoltaic applications of upconversion nanomaterials.

1. Introduction

Global energy consumption is keep on raising and expected to double by the end of 2050. Most of our energy supply comes from fossil fuels; however, the finite nature and the environmental concerns associated with fossil fuels, triggered the search for alternative renewable energy sources.[1,2] There exist many potential renewable energy technologies such as biomass, geothermal, hydrogen fuel cell, hydropower, ocean, wind and solar. Sunlight is a freely available abundant source of solar energy and irradiates the Earth's surface with one hundred and twenty thousand terawatts of solar power. It has been reported that the Earth's surface receives nearly 10,000 times more sunlight than what we consume.[3] Harnessing solar energy through photovoltaic (PV) technology has the potential to meet our energy demands in a cleaner way.

Solar cell is a photovoltaic device that converts the light photons directly into electricity. Solar cells are anticipated to make a sustainable future with biggest energy economy through the development of solar energy technology. Environmental benign solar cells are essentially required to power the electricity demanding areas ranging from portable electronics to transportation and stationary. In general, solar cells are divided into different generations namely first, second and third generations.[4] Both single-crystalline and poly-crystalline silicon wafers have been primarily used for fabrication of first-generation solar cells. Silicon solar cell technology is the well grown and most utilized system achieving a best efficiency of 25%. Unfortunately, they are expensive to produce and the market cost is dominated by the expensive purification cost of silicon substrates.[5] The second generation solar cells have been developed to move away the usage of high cost materials. The second generation mainly based on thin film solar cells that are produced cheaply, such that the cost per watt is lower than the first generation cells. Thin film solar cells such as CIGS (Cu, In, Ga, Se_2), CdTe, and amorphous silicon are most popular in second generation and have best cell efficiencies of 20.8%, 20.4%, and 13.4% respectively. Nevertheless, the efficiency of thin film solar cells is still lower than first generation silicon cells and several second generation cells rely on scarce and toxic materials.[6] Both first and second generation solar cells are suffered from the Shockley-Queisser limit, which states that a single-junction solar cell with band gap equal to 1.1 eV can only have a maximum efficiency of 31%.[7] Third generation solar cells have the potential to overcome the Shockley-Queisser limit and are considered as potential alternative to expensive first and toxic second generation solar cells. They are inexpensive, have simple fabrication process and importantly can be printed on large area and flexible substrates. This comprises of solar cell technologies such as Dye-sensitized solar cells (DSSCs),[8,9] colloidal quantum dot solar cells,[10] organic photovoltaics[11,12] and solution processed bulk inorganic photovoltaics, *etc*.[13] Most of the third generation technologies are not yet commercialised, but there is a lot of research going on in this area. In third and present generation, the goal is under way to make inexpensive solar cells with high efficiency.

For any single junction solar cell, the band gap (E_g) of the semiconductor which used to construct the solar cell, determines the maximum conversion efficiency.[14] Fig. 1 shows the schematic diagram of the loss mechanisms that affect the efficiency of single-junction solar cells. There are two major loss mechanisms which need to be addressed to enhance the solar cell efficiencies are lattice thermalisation and transparency to sub band gap photons. When a semiconductor absorbs a photon of higher energy than the band gap, electron–hole (e–h) pair with higher energy is created and the excess energy is dissipated as heat. This is known as thermalisation loss. On the other hand, photons with energy lesser than the band gap are not absorbed by the semiconductor and are

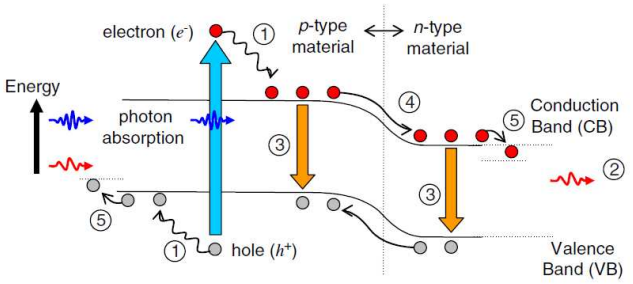

Fig. 1 Loss processes in a single-junction solar cell: (1) lattice thermalisation loss; (2) transparency; (3) recombination loss, (4) junction loss and (5) contact voltage loss. Reprinted with permission from Ref 14. Copyright 2006, Elsevier.

transmitted. Thermalisation losses are high in solar cells with smaller bandgap, whereas, transmission losses contribute more to the losses for wider band-gap solar cells. A further loss mechanism is the recombination of e-h pairs close to or at the surface, and this loss process can be minimized through maintaining high minority carrier lifetimes in the semiconductor material. About 70% of the energy loss is related to thermalisation and transmission energy losses, and are termed as spectral mismatch. These are mainly resulted from the spectral mismatch between the incident solar spectrum and the band gap of the semiconductors.

In order to tackle the spectral mismatch, solar cells with a series-connect stack of two-five junctions (Multi-junction solar cells) made from semiconducting materials with a decreasing band gap are proposed. A multi-junction solar cell that covers a range of the solar spectrum with different wavelengths have greatly increased the efficiency of solar cell, and almost reached twice the efficiency of the single junction cells. Compared to all other single-junction solar cells, multi-junction solar cells have the highest theoretical limit of efficiency and produced maximum recorded efficiency of 43.5%.[15] However, multi-junction solar cells are much more complex than the single junction versions. This increased complexity, greatly increases the production cost and it is relatively expensive for globalization. Thus, the single junction solar cells are most commonly used in present days. Many strategies are under investigation for achieving efficient light absorption, charge separation, transport and collection in single junction solar cells.[16-18] Even though many light harvesting methods available for trapping the wide range of solar spectrum, still there is a need for enhanced photon absorption technology for the development of high efficiency solar cells.

The wavelength conversions of light photons are a promising route to reduce spectral mismatch losses that are considered to be the major part of the efficiency losses in single junction solar cells. In recent years, wave length dependent spectral convertors are explored for enhanced energy conversion in single-junction solar cells. There are three luminescence processes namely, quantum cutting, downshifting and upconversion, have the potential to increase the solar cell efficiencies. Quantum cutting through down conversion is able to cut one high energy photon into multiple low energy photons with a conversion efficiency higher than 100%.[19] Quantum cutting reclaims some of the excess energy of high energy photons through down conversion process and down converted photons can be absorbed by solar cells which minimize the energy loss and increase the conversion efficiency. A subcategory of down conversion is downshifting process that occurs at sub-unity quantum efficiencies and involves transformation of one absorbed high energy photon into one lower-energy photon. Both downshifting and quantum cutting are interrelated, but in the case of downshifting, the efficiency cannot exceed 100%. Downshifting can effectively convert short wavelength ultraviolet light to longer wavelength visible light, for which the solar cells have maximum response.

Upconversion is a process where low energy photons (infrared and near infrared) are converted into high energy visible photons. This process could enable the conversion of incident light with energies smaller than the semiconductor band gap and can significantly reduce the transmission energy losses. In 2002, Trupke and Green *et al.*[20] proposed that the upconversion of sub-bandgap light can result in significant improvements of the conversion efficiency of solar cells. They investigated a system of bifacial silicon solar cell with upconversion layer placed on the rear side. The upper limit of the energy conversion efficiency of the system was found to be 63.2% for concentrated sunlight and 47.6% for nonconcentrated sunlight. This model boosted the research on upconversion solar cells.

In this review, we focus on the light absorption enhancement of single junction solar cells through selective upconversion process. First, we describe the basic concepts of upconversion luminescence. Second, we describe the recent developments on the synthesis of various upconversion nanomaterials by the thermal decomposition method, hydro/solvothermal method, co-precipitation method, microwave-assisted method, and ionic-liquid-based synthesis. Third section describes some important strategies to improve the upconversion photoluminescence. Finally, we highlight the recent research progress on the application of upconverter materials in various solar cells such as, crystalline silicon, amorphous silicon, DSSC and organic solar cells. The summary of the present review will make the positive insight on the topic of upconversion nanomaterials application in solar cells.

2. Upconversion Luminescence

2.1. Upconversion mechanism

Upconversion (UC) is a unique type of photoluminescence in which lower energy excitation (near-infrared light) is converted into higher energy emission (visible light) via multi-photon absorption processes. This phenomenon was first discovered by Auzel in the 1960s.[21] Generally, UC process is observed in lanthanide or transition metal ions doped in an inorganic host and to some extend in organic chromophores with an extended conjugated π-system.[21-23] UC processes can be mainly divided into three broad classes: excited-state absorption (ESA), energy transfer

upconversion (ETU), and photon avalanche (PA). All these processes involve the population of highly excited state by sequential absorption of two or more photons by metastable, long-lived energy states.

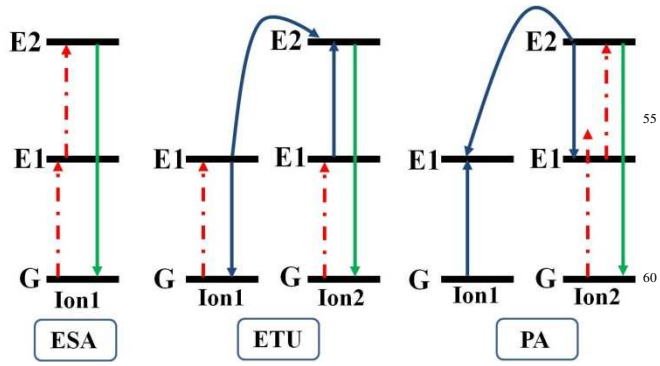

Fig. 2 Principle upconversion processes in lanthanide (Ln^{3+}) doped upconversion nanomaterials.

In excited state absorption, a single emitting ion with ladder like energy levels sequentially absorbs two (or more) photons using a real intermediary energy level, and promoted to a higher excited state. The general energy diagram of the ESA process is shown in Fig. 2 for a simple three-level system. The energy difference between the level G and E1 is similar to that of level E1 and E2, which facilitates the ESA mechanism. When the excitation energy is resonant with the transition from ground level G to excited metastable level E1, a process known as ground state absorption (GSA) takes place and populates the E1 level. The ion in E1 level has a high possibility to be promoted to E2 level by another pump photon due to the long lifetime of E1 state, before its decay to the ground state. The upconversion emission occurs from the E2 level.

Energy transfer upconversion is quite different from the ESA, as ESA is operated within a single lanthanide ion, while ETU involves two neighbouring ions. In an ETU process, each of two neighbouring ions can absorb a pump photon of the same energy by GSA, thereby populating the metastable level E1. A non-radiative energy transfer, promotes one of the ions to upper emitting state E2, while the other ion relaxes back to ground state G. The upconversion efficiency of an ETU process is highly sensitive to the average distance between the neighbouring two ions, which is determined by the concentrations of dopants.

Chivian and co-workers were first discovered the phenomenon of photon avalanche in Pr^{3+} infrared quantum counters.[24] PA is a process that produces UC above a certain threshold of excitation power. It is a looping process which involves processes of ESA for excitation light and an efficient cross relaxation (CR) that produces feedback. First, E1 level of ion 2 is populated by weak non resonant GSA, followed by resonant ESA to populate the level E2. An efficient CR energy transfer occurs between the excited ion 2 and a neighbouring ground state ion 1, resulting in both ions occupying the intermediate level E1. Last, ion 1 transfers its energy to ion 2 to populate its E1 level and completes the loop. The net result produces two ion 2's at E1 level. One of them absorbs the excitation radiation and is excited to the E2 state, in which it interacts with ground state of ion 1 by CR form three ion 2's at E1 level. By repeating the whole steps again and again, the E2 level of ion 2 is increasing dramatically and produces strong UC emission.

2. 2. Upconversion in Lanthanide ions

A typical inorganic UC phosphor contains a crystalline host material and a dopant (emitter) added in low concentration. The dopant acts as luminescent centers while the host provide a crystalline matrix to bring these centers into optimal position. The presence of multiple meta-stable levels in lanthanide ions makes them as a preferred dopant for UC inorganic phosphors. The lanthanides, which are characterized by the progressive filling of the 4f orbitals, are a family of 15 chemically similar elements, commence with lanthanum (La) and end with the lutetium (Lu). Lanthanide ions typically exist in their most stable oxidation state as trivalent ions (Ln^{3+}) and have a $4f^n5s^25p^6$ electron configuration ($0< n >14$). Their characteristic optical and magnetic properties arises as a result of the partly filled 4f inner shell. There are 14 over n possible configurations available for lanthanide ions with n number of electrons. This results in a fairly large number of energy levels structures.[25] Most of the Ln^{3+} ions show sharp f-f transition bands due to the fact that 4f electrons of Ln^{3+} ions are shielded by the completed filled $5s^2$ and $5p^6$ sub-shells. The transitions between different $4f^n$ states are Laporte forbidden, which results in low transition probabilities and substantially long-lived (up to 0.1 s) excited states.[21] Since the excited states of lanthanide ions have longer life times, an excited lanthanide ion may sequentially absorb a second photon of suitable energy at comparatively low excitation densities and reach an ever-higher excited state. When the energy gap between three or more subsequent energy levels in lanthanide ions are very similar, then they can be excited higher excited state using monochromatic light source, since each absorption step requires the same photon energy. In this sense, Er^{3+}, Tm^{3+}, and Ho^{3+} ions, featuring ladder-like energy levels were generally chosen as emitters to give rise to efficient UC emission.[26] For example, in Er^{3+} ion the energy difference between the $^4I_{11/2}$ and $^4I_{15/2}$ states (~ 10350 cm^{-1}) is similar to that between the $^4F_{7/2}$ and $^4I_{11/2}$ states (~ 10370 cm^{-1}). In addition, energy difference between the $^4F_{9/2}$ and $^4I_{13/2}$ states is in the same region, and hence the Er^{3+} ion can be excited to higher energy level by at least three possible transitions by absorbing the IR photons of same energy, which gives the visible upconverted green and red emissions (Fig. 3).

In singly doped UC phosphor, there are two limiting factors which affect the UC emission intensity are the distance between two neighbouring emitting ions and the absorption cross-section of the ions. The absorption can be increased by increasing the emitter's concentration in phosphors, but at higher dopant concentration cross-relaxation may be a severe problem which quenches the excitation energy. In most of the UC materials the Er^{3+} and Tm^{3+} concentration does not exceed 3 and 0.5 %, respectively. At this low concentration, Er^{3+} and Tm^{3+} ions cannot absorb the excitation light effectively, which results in low UC efficiency.

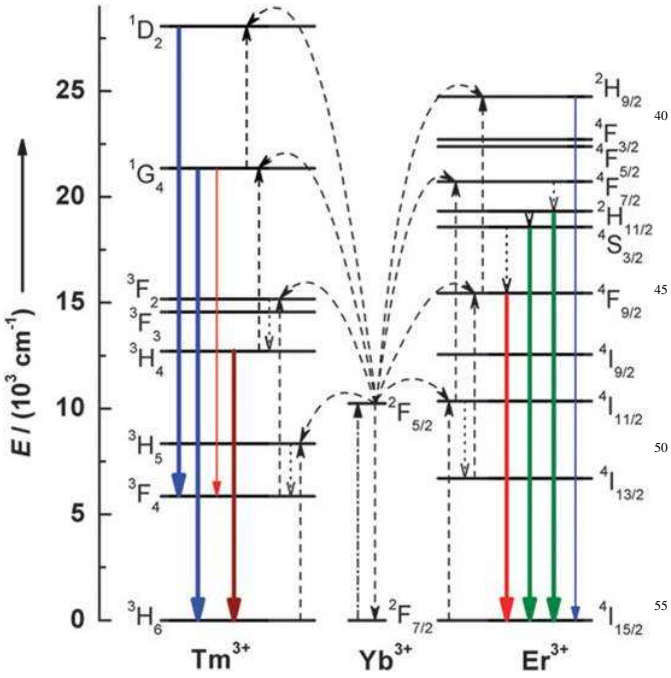

Fig. 3 Proposed energy transfer mechanisms showing the UC processes in Er^{3+}, Tm^{3+}, and Yb^{3+} doped crystals under 980 nm diode laser excitation. The dashed-dotted, dashed, dotted, and full arrows represent photon excitation, energy transfer, multiphonon relaxation, and emission processes, respectively. Only visible and NIR emissions are shown here. Reproduced from Ref. 26 with permission from The Royal Society of Chemistry.

In order to increase the absorption in lanthanide-doped phosphors, a sensitizer with a sufficient absorption cross-section in the NIR region is usually co-doped along with the emitting ion. Trivalent ytterbium (Yb^{3+}) is the most commonly used sensitizer for UC phosphors. Yb^{3+} has an extremely simple energy level scheme with only one excited 4f level of $^2F_{5/2}$. The Yb^{3+} has a larger absorption cross section than any other lanthanide ions, and the absorption band is located at 980 nm. In addition, the $^2F_{7/2} \longrightarrow {}^2F_{5/2}$ transition of Yb^{3+} is well resonant with transition energy between the $^4I_{11/2}$ and $^4I_{15/2}$ states and also the $^4F_{7/2}$ and $^4I_{11/2}$ states of Er^{3+} ions, thus facilitating the energy transfer from Yb^{3+} to Er^{3+} ions. Usually higher concentration of Yb^{3+} sensitizer is doped in UC materials (18-20%). Yb^{3+} is also standard sensitizer for Tm^{3+} and Ho^{3+} ions.

Lanthanide emitters and sensitizers are generally embedded in a host matrix to fabricate upconversion phosphors. The choice of host matrix has strong influence on the upconversion process, since the distance between the dopant Ln^{3+} ions, their relative spatial position, their coordination numbers, and the type of anions surrounding the dopant are determined by the host lattice. Halides such as fluorides, chlorides, bromides, iodides and oxides such as silicates, borates or phosphates are usually serve as host to construct upconversion phosphors. Ideal host materials should have low lattice phonon energies and good stability. Generally halides exhibit low phonon energies but the hygroscopic nature of halides limited their use. Whereas oxides are very stable but their phonon energies are relatively high than 500 cm^{-1}.[27,28] The most promising host for upconversion phosphors are found in fluoride materials owing to their low phonon energy (ca. 350 cm^{-1}), high refractive index, and good thermal stability.[29,30]

3. Synthesis of upconversion nanomaterials

3.1. Thermal decomposition:

Thermal decomposition method involves the decomposition of organometallic precursors in high boiling point organic solvents in the presence of long alkyl chain surfactants. Decomposition normally takes place at elevated temperatures (300 to 350 °C). Most frequently used organometallic precursors are metallic trifluoroacetate salts and rare-earth oleates; the solvent is 1-octadecene (ODE); the surfactants can be oleic acid (OA), oleylamine (OM) or trioctylphosphine oxide (TOPO). Thermolysis method produces high quality UC nanocrystals with uniform size distribution, high crystallinity and exceptional optical properties.

3.1.1. Trifluoroacetate precursors

Yan and co-workers first developed the thermal decomposition method to synthesis highly monodisperse LaF_3 triangular nanoplates from a single-source precursor $La(CF_3COO)_3$ in OA/ODE at 280 °C.[31] This method was later developed as a common route to synthesize other kinds of RE-based NCs. For example, Capobianco and co-workers reported the synthesis of cubic $NaYF_4$ nanoparticles codoped with Yb/Er or Yb/Tm, with broad size distribution (10 - 60 nm).[32] They further refined the procedure to synthesize nanoparticles with a regular shape and a monodisperse particle size distribution.[33] It was found that the slow addition (ca. 1mL/min) of precursor solution is the key to synthesize monodisperse nanoparticles. In the mean time, Yan and co-workers pioneered the general synthesis of high-quality α/β-$AREF_4$, (A = Na, Li, K, and RE = Pr - Lu, Y) NCs via the co-thermolysis of $A(CF_3COO)$ and $RE(CF_3COO)_3$ precursors in the mixed solvent of OA-OM-ODE (Fig. 4e-h).[34-36] In this work, pure α-$NaREF_4$ NCs were produced at low temperatures (250-290 °C) and low ratios of Na/RE, while β-$NaREF_4$ NCs were obtained at higher temperatures (330 °C) and high Na/RE ratios. They found that the α → β phase transition is closely correlated with the particle size. Accordingly, the size and shape selective synthesis can be carried out by controlling the thermodynamic or kinetic growth of the NCs. Murray and co-workers demonstrated the advantage of thermal decomposition method by preparing hexagonal $NaYF_4$ nanoparticles in diverse shapes such as spherical NPs, nanorods, hexagonal nanoprisms and nanoplates (Fig. 4i-l).[37] Apart from ODE, oleylamine can also be used as solvent to prepare UCNPs by thermolysis method. Chow et al. reported the synthesis of small β-$NaYF_4$:Yb,Er nanoparticles in pure oleylamine solvent.[38] In this method the oleylamine acts as both the solvent as well as co-ordinating ligand.

Table 1. Typical upconversion host materials and their synthetic methods

Thermal decomposition

Host	Shape	Size distribution (nm)	Ref
$NaYF_4$	sphere, nanorod, nanocube, nanoplate, nanoprism	15-60 narrow	33,35,37,38, 74,75
$NaGdF_4$	sphere	2-30 narrow	35,57,76-78
$NaYbF_4$	sphere, polyhedron	15-60 narrow	35, 60, 79
$NaScF_4$	sphere, hexagonal	20-40 narrow	80, 81
$NaREF_4$ (RE = Nd, Sm, Eu, Tb, Dy, Ho, Er, Tm, Lu)	sphere, nanorod	10-150	35
$LiREF_4$ (RE = Tb - Lu, Y)	polyhedron, rhombic nanoplate	20-90 narrow	36
$KREF_4$ (RE = La to Gd, Y)	nanowire, nanocube and nanopolyhedra	7-20 narrow	36
REF_3 (RE = Y, La, Ce, Pr, Nd, Sm, Eu, Gd, Tb, Dy, Ho, Tm, Yb, Lu)	nanoplate, sphere, nanozigzag, truncatedoctahedron, nanorod, nanopolyhedra rhombic nanodisk	5-20 narrow	31, 82,83
MF_2 (M= Mg, Ca, Sr, Ba)	sphere, nanoneedle, nanoplate, nanowire,	3-100 narrow	84,85
MFCl (M= Ca, Sr, Ba)	nanocube	12-20 narrow	86
$KMnF_3$	nanocube	10-40 narrow	87
$NaMnF_3$	sphere	8-10 narrow	88
RE_2O_3 (RE= Y, Gd,	nanoplate, nanodisck	5-10 narrow	47-49
YOF	nanosphere	14-16 narrow	89

Hydro(solvo)thermal method

Host	Surfactant	Shape	Ref
$NaYF_4$	OA	sphere, nanoplate, nanorod, nanotube, nanodisk	97-100, 102,122
	Cit^{3-}	microplate	109-111
	EDTA	sphere	113
	PVP	sphere	115
	PEI	sphere	117-120
	PAA	nanorod	121
$NaGdF_4$	OA	Sphere, polyhedron	104,122
$NaREF_4$ (RE = Pr, Nd, Sm, Eu, Dy, Ho, Er, Tm, Tb	OA	polyhedron, nanotube, nanodisk, nanorod	122
$KGdF_4$	PEI, 6-aminocaproic acid (6AA)	sphere	123
$BaYF_5$	EDTA	sphere	114,124
	PEI	sphere	125
BaY_2F_8	OA	nanobelt	106
Ba_2GdF_7	EG	pseudo-octahedron	126
Ca_xYF_{3+2x}	CTAB	micro-cubic and rhombic	127
CaF_2	OA	sphere	101
SrF_2	OA	sphere	103

MnF_2	OA	nanoclusters and nanolanterns	108
ErF_3	Cit^{3-}, EDTA, PVP, CTAB	flower-like, microcrystal	128
$PbTiO_3$	Polyvinyl alcohol	nanofiber	109
GdF_3	PVP	sphere	130
$GdVO_4$	PVP	sphere	131
Gd_2O_3	-	sphere	132
La_2O_3	-	triagonal or truncated triagonal-prism/plate, hexagonal prism	133
Gd_2O_2S	PVP	submicrosphere	134
Precipitation method			
$NaYF_4$	EDTA	sphere	136
REF_3 (RE = Eu, Er, Nd, and Ho)	ammonium di-*n*-octadecyldithioposhate	elongated particle	135
$NaGdF_4$	Na_2EDTA, PVP, SDS, Na_2tar	rod shape aggregate	137
LaF_3	ammonium di-n-octadecyldithiophosphate	sphere	138
Lu_2O_3	urea	nano-aggregate, sub-micrometer wire, and nanosphere	139
Y_2O_3	CTAB	sphere	140
Microwave synthesis			
$NaYF_4$	OA	hexagonal and cubic	142
	-	sphere, bipyramidal microdisk	143,144
$NaGdF_4$	PEI	quadral cubic, popcorn like hexagonal	145
$BaYF_5$	PEI	sphere	146

The synthesized nanoparticles were uniform in shape, and showed a narrow size distribution (10.5 ± 0.7 nm). Shan et al. first reported the use of trioctylphosphine oxide (TOPO) as a replacement for the most frequently used capping agents such as OA, and OM.[39-41] The as-synthesized NCs had controllable sizes in the range 5 - 20 nm with narrow size distribution. But they suffer from the low solubility in common organic solvents like cyclohexane or chloroform. This problem was later solved by replacing TOPO with using TOP/OA mixture.[40,41]

3.1.2. Rare-earth oleate and acetate precursors

Though trifluoroacetate precursors offer many advantages, the release of toxic fluorine species from the thermal decomposition of trifluoroacetates makes them less attractive. Therefore, efforts were made to develop alternative synthetic methods that also allow control over the crystal phase, shape, and size of the particles.

Chen and co-workers reported a non toxic thermolysis method for the preparation of β-$NaYF_4$ and $NaGdF_4$ NCs. This method involves the reaction of RE oleate ($RE(OA)_3$) complex and NaF in OA/ODE solvent. By simply changing the ratios of NaF-to-$RE(OA)_3$, the sizes of the β-$NaYF_4$:Yb,Er/Tm NPs can be tuned from larger nanoplates to smaller nanospheres of size about 18 nm.[42-44] Recently, Na et al. controlled the morphology of β-$NaYF_4$:Yb,Er/Tm NPs from large spheres (37.9 nm) to rods (length = 60.1 nm, width = 21.5 nm) and from rods to hexagonal prisms (length = 48.8 nm, width = 44.0 nm).[45] When OA/ODE ratio was 2:19 large spheres (Fig. 5a, b) were produced, whereas nanorods were obtained with 19:2 ratio (Fig. 5c). By adding 2.5 mmol NaCl the nanorods were transformed to hexagonal prisms (Fig. 5d). RE-oleate method was later extended to synthesis other fluoride NCs, including REF_3 (RE = La - Pr), $NaREF_4$ (RE = Sm - Er), and $Na_5RE_9F_{32}$ (RE = Tm - Lu) with diverse morphologies.[46] Besides fluoride nanocrystals, $RE(OA)_3$ complexes can also be used to synthesize RE oxide nanostructures.

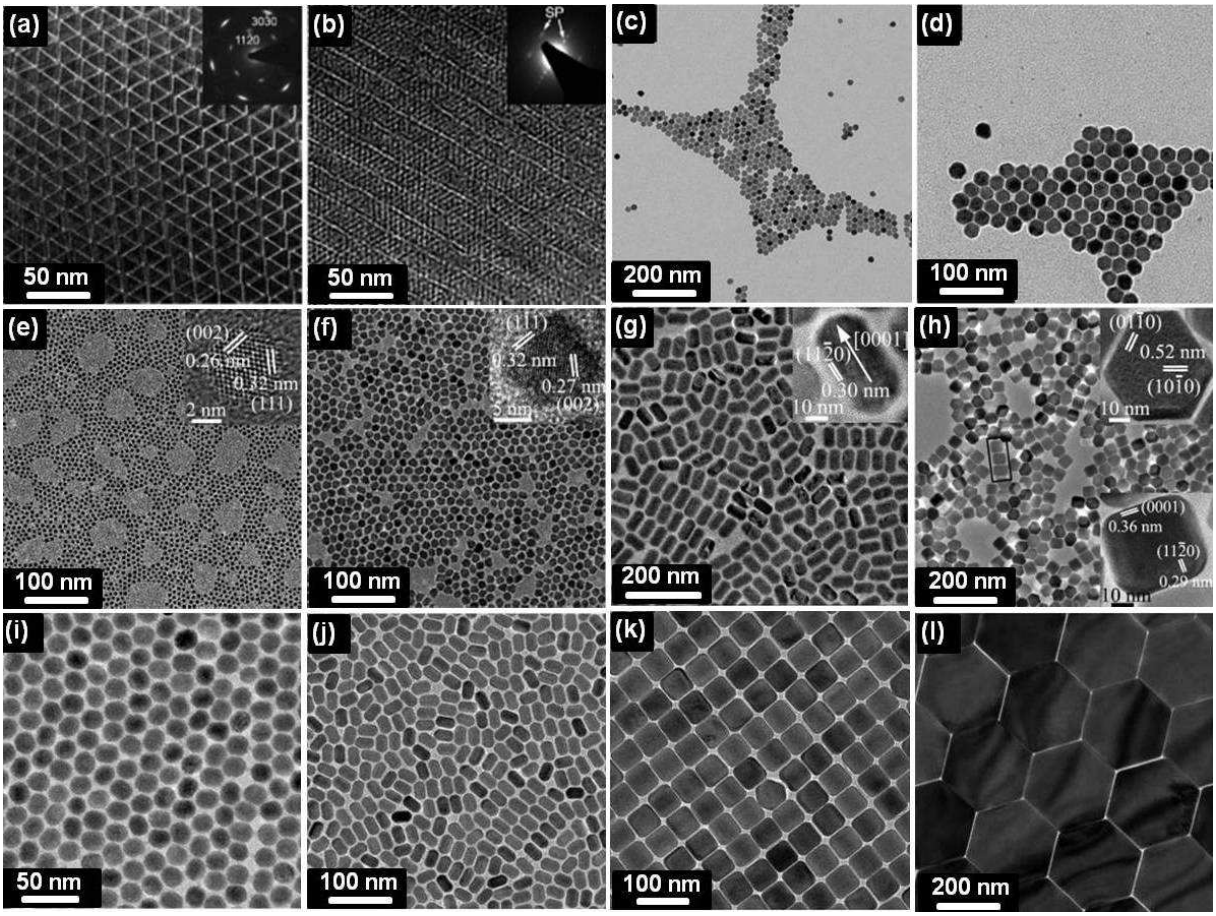

Fig. 4 TEM images of (a, b) LaF_3 nanoplates, (c, d) $NaYF_4$:Yb,Er nanoparticles, (e) α-$NaNdF_4$, (f) α-$NaYF_4$ nanoparticles (g) β-$NaYF_4$ nanorods, (h) β-$NaHoF_4$ hexagonal plates. (i-l) TEM images of β-$NaYF_4$:Yb,Er (i) spherical nanoparticles, (j) nanorods, (k) hexagonal nanoprisms and (l) hexagonal nanoplates. Reprinted with permissions from Ref 31, 33, and 35 (copyrights 2005, 2007, and 2007 American Chemical Society) and 37 (copyright, 2010 National Academy of Sciences).

Tan and co-workers synthesized several doped RE_2O_3 (RE = Y, Gd) nanodots and nanorods by the decomposition of $RE(OA)_3$ precursors in OM solvent (Fig. 5e, f).[47,48] In this method, the first formed nanodots were self-assembled to nanorods with same diameter by increasing the reaction time from 10 min to 2 h. The self assembly process was attributed to dipole-dipole interactions. Other RE complex salts such as acetate ($RE(Ac)_3$), acetylacetonate ($RE(acac)_3$), and benzoylacetonate have been used to synthesis RE oxide nanostructures. Murray and co-workers synthesized tripodal and triangular Gd_2O_3 nanoplates with a thickness of 2 nm using gadolinium acetate precursor in OA/OM/ODE mixture (Fig. 5g, h).[49] Yan and co-workers explored the preparation of RE oxide nanoplates using $RE(acac)_3$ and RE benzoylacetonate as precursors.[50,51]

3.1.3. Ostwald-Ripening strategy

In 2008 Li and Zhang reported a facile and user-friendly method for the synthesis of pure β-$NaYF_4$ nanocrystals in OA and ODE at 300 °C. In this method the trifluoroacetate and RE oleate precursors were replaced with $RECl_3$, and NaOH and NH_4F were used as Na^+ and F^- source, respectively.[52] The particles were of high quality in terms of size distribution (average size 21 nm) and shape uniformity (nanospheres and hexagonal plates depending on the amount of oleic acid) (Fig. 5i-l). Two major steps involved in this method; (1) formation of small amorphous sacrificial $NaYF_4$ co-precipitates at room temperature (2) particle growth *via* the Ostwald ripening mechanism at elevated temperature (300 °C). To date, a series of monodisperse doped RE fluoride nanoparticles including $NaYF_4$,[53-56] $NaGdF_4$,[57] $NaLuF_4$,[58] $NaDyF_4$,[59] and $NaYbF_4$[60] have been synthesized using this method. Furthermore, this method is well suited for the synthesis of core-shell and core-shell-shell structures with uniform morphology and size by a seeded growth approach. Various core-shell nanostructures including $NaYF_4$:Yb,Ln@$NaYF_4$ (Ln = Er, Tm, Ho),[61-65] $NaGdF_4$:Yb,Er/Tm@$NaGdF_4$,[66] KYF_4:Yb,Er@KYF_4,[67] $KGdF_4$:Yb,Tm@$KGdF_4$,[68] $NaYF_4$:Yb,Er@$NaGdF_4$,[69-71] $NaGdF_4$:Yb,Tm@$NaYF_4$,[62] $NaYbF_4$:Tm@$NaGdF_4$,[60] $NaYF_4$:Yb,Tm@$NaYF_4$:Yb,Er,[72] and core-shell-shell nanostructures such as $NaYF_4$:Yb,Tm@$NaYF_4$:Yb,Tm@$NaYF_4$,[73] $NaYF_4$:Yb,Tm@$NaYF_4$:Yb,Er@$NaYF_4$:Yb,Tm[72] have been successfully synthesized.

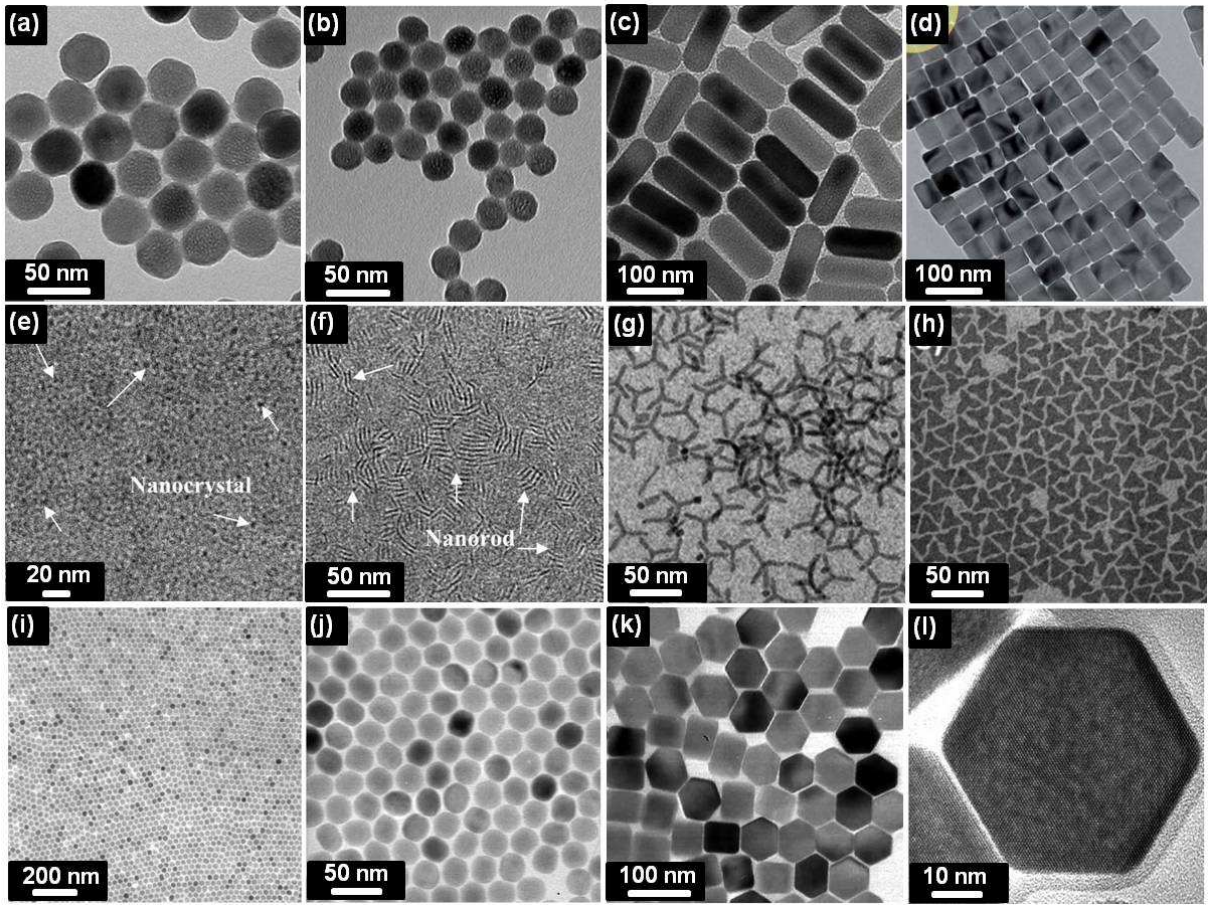

Fig. 5 TEM images of β-$NaYF_4$:Yb,Er (a, b) nanoparticles, (c) nanorods, (d) hexagonal prisms. TEM images of Y_2O_3:RE nanodots and nanorods obtained at 280 °C after (e) 10 min, and (f) 2 h. TEM images of tripodal and triangular Gd_2O_3 nanoplates synthesized at (g) 280 and (h) 310 °C for 1 h. TEM images of $NaYF_4$:Er,Yb (i, j) nanospheres and (k, l) nanoplates at different magnifications. Reprinted with permissions from Ref 45 (copyright 2013, The Royal Society of Chemistry), 47, 49 (copyrights 2008, 2013 American Chemical Society), and 52 (copyright 2008, IOP Publishing).

At present, the thermal decomposition and Ostwald ripening methods are becoming the most common method for the synthesis of high quality UCNPs. However, some inherent disadvantages still need to be addressed. First, the rigorous and harsh experimental conditions (high temperature, waterless, oxygen-free and inert gas protection). Second, the use of expensive solvents and the toxic nature of the by-products from trifluoroacetate. Third, the nanoparticles are soluble only in non polar solvents or weak polar solvents. Therefore post synthesis treatment is needed to make them soluble in common polar solvents such as water and ethanol.

3.2. Hydro(solvo)thermal methods

The hydro(solvo)thermal synthesis utilizes a solvent under pressures and temperatures above its critical point to increase the solubility and reactivity of precursors and allow fine crystallization of the final products. Generally, the reactions are carried out in specialized reaction vessels known as autoclaves, which consists of an inner Teflon liner, an outer stainless steel shell, and a stainless steel cap. The products obtained by hydro(solvo)thermal method usually exhibit high crystallinity and few defects. The hydro(solvo)thermal synthesis provide obvious advantages such as (1) higher yield and purity (2) relatively low reaction temperature (usually below 220 °C) (3) well controlled size, structure and morphology of the final product. Based on the reaction conditions hydro(solvo)thermal methods can be broadly divided into three classes. (1) organic-additive free synthesis (2) hydrophobic ligand assisted synthesis, and (3) hydrophilic ligand assisted synthesis.

3.2.1. Organic-additive free hydro(solvo)thermal synthesis

This method provides straight forward route to synthesis 1D nanowires, nanorods, nanotubes without any organic additives and templates. Wang and Li synthesized $RE(OH)_3$ (RE = Y, La, Nd, Sm-Tm) nanowires in basic solution with NaOH or KOH as precipitator at hydrothermal temperature of 180 °C.[90,91] They also obtained $RE(OH)_3$ (RE = Y, La-Yb) nanotubes with open ends by lowering the temperature to 120-140 °C.[90,92] Furthermore, RE oxide, oxyfluoride, and oxysulfide nanowires/ nanotubes were prepared by calcination, fluoridation, and sulfidation of the as prepared hydroxide nanowires/nanotubes. Zhang and Zhao reported the synthesis of rare-earth fluoride β-$NaREF_4$ nanotubes

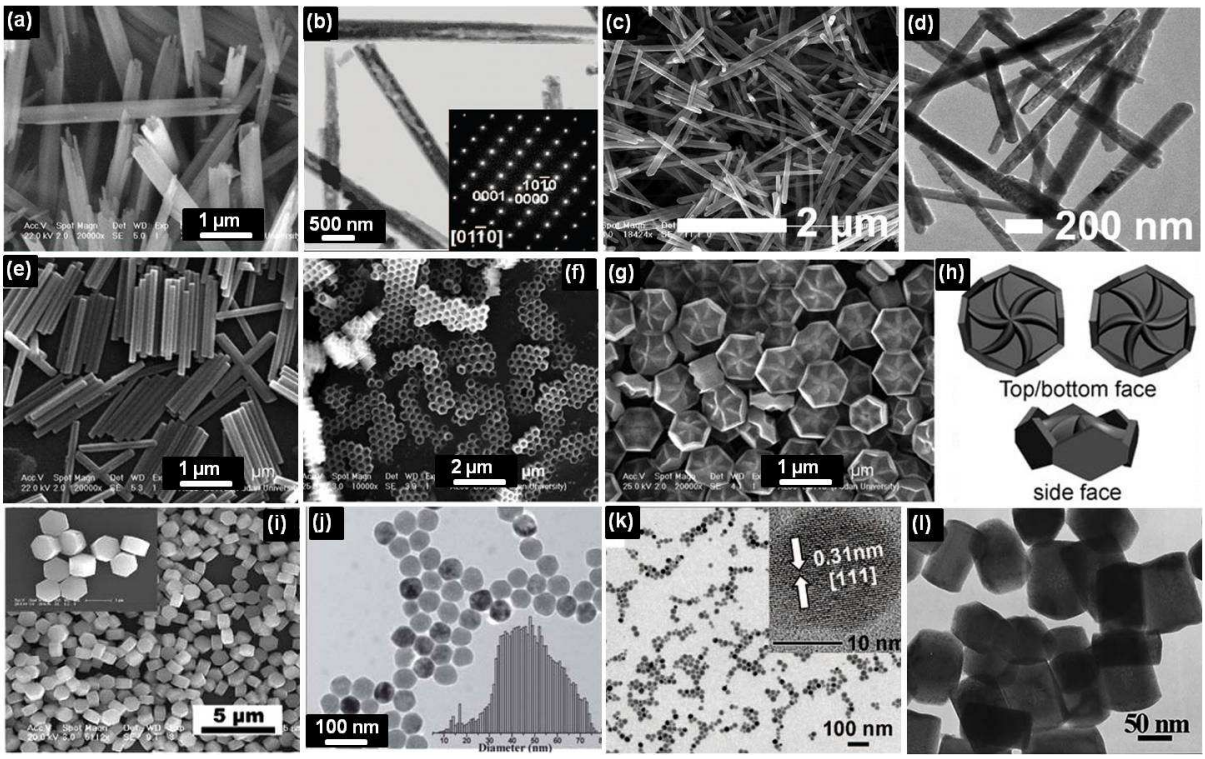

Fig. 6 (a) SEM image of $Y(OH)_3$ nanotubes (b) TEM image of $NaYF_4$ nanotubes. (c) SEM image of $Y(OH)_3$ nanowires, (d) TEM image of $NaYF_4$ nanowires synthesized using organic-additive free hydro(solvo)thermal synthesis. SEM images of arrays of β-$NaYF_4$ (e) nanorods, (f) nanotubes and (g) flower-patterned hexagonal disks. (h) Illustration of the {0001} top/bottom faces and the {1-100} side faces of a disk. (i) SEM image of β-$NaYF_4$:Tb hexagonal microplates synthesized using Cit^{3-} (j) TEM image of $BaYF_5$ nanocrystals synthesized using EDTA, (k) TEM image of $NaYF_4$:Yb,Er nanoparticles obtained using PEI and (l) $NaYF_4$:Yb,Er nanocrystals synthesized using PAA. Reprinted with permissions from Ref 93, 94 (copyright 2008, 2009 American Chemical Society), 99 (copyright 2007, Wiley-VCH Verlag GmbH & Co. KgaA), 109 (Copyright 2007, American Chemical Society), 114 (copyright 2011, The Royal Society of Chemistry), 118 (Copyright 2008, American Chemical Society), and 121 (copyright 2012, The Royal Society of Chemistry).

via hydrothermal in situ ion-exchange reaction by using rare earth hydroxides [$RE(OH)_3$] as a parent (where RE = Y, Pr, Sm, Gd, Tb, Dy, and Er).[93] In this method, NaF and HF were reacted with $RE(OH)_3$ precursors at 120 °C for 12 h. During this process, HF diffuses into single-crystalline $RE(OH)_3$ nanotubes, F^- ions can substitute the OH^- ions and interact with RE^{3+} ions to form the more stable β-$NaREF_4$ phase (Fig. 6a,b). Similarly, Xu et al. synthesized nearly monodisperse and well-defined one-dimensional (1D) rare earth fluoride (β-$NaREF_4$) (RE=Y, Sm, Eu, Gd, Tb, Dy, and Ho) nanowires/nanorods (Fig. 6c,d).[94]

3.2.2. Hydrophobic ligand assisted hydro(solvo)thermal synthesis

In 2005, Li and co-workers developed a facile solvothermal method for preparing hydrophobic NCs using liquid-solid-solution (LSS) strategy.[95] This method is based on a general phase transfer and separation mechanism occurring at the interfaces of the ethanol -linoleic acid liquid phase (liquid), metal linoleate (solid), and water - ethanol solution containing metal ions (solution). The schematic diagram for LSS method is illustrated in Fig. 7. In the case of $NaREF_4$ nanocrystals synthesis, the phase transfer process across the solid phase and solution transfers RE^{3+} ions to solid phase as RE linoleate $(RCOO)_nRE$ complex. Under designed reaction conditions, the reaction between NaF and $(RCOO)_nRE$ produces $NaREF_4$. Using this method with slight modification, variety of UCNPs with well-controlled crystal phase, size, and shape have been synthesized.[96-108] For example, Zhao and co-workers utilized oleic acid-mediated hydrothermal method for the synthesis of Yb and Er doped $NaYF_4$ nanorods, nanotubes, and flower-patterned nanodisks (Fig. 6e-h).[99] Employing a similar synthetic system, Liu and co-workers studied the effect of RE^{3+} doping on the crystal phase, size, and optical properties of the $NaYF_4$ UCNPs. They found that RE^{3+} doping at precisely defined concentrations controlled the sizes (down to 10 nm), phases (cubic or hexagonal), and UC emission colors (green to blue).[102] Recently, Tian et al. used LSS method to synthesis Mn^{2+} doped $NaYF_4$:Yb,Er UCNPs. It was found that without Mn^{2+} ions, the synthesized nanoparticles were mixed phase (hexagonal and cubic) and had two different morphologies that include small nanocubes (cubic phase) and larger hexagonal nanorods (hexagonal phase). When 30 mol% Mn^{2+} ions were doped, single cubic phase and smaller (~ 20 nm) $NaYF_4$:Yb,Er nanoparticles were obtained.[105]

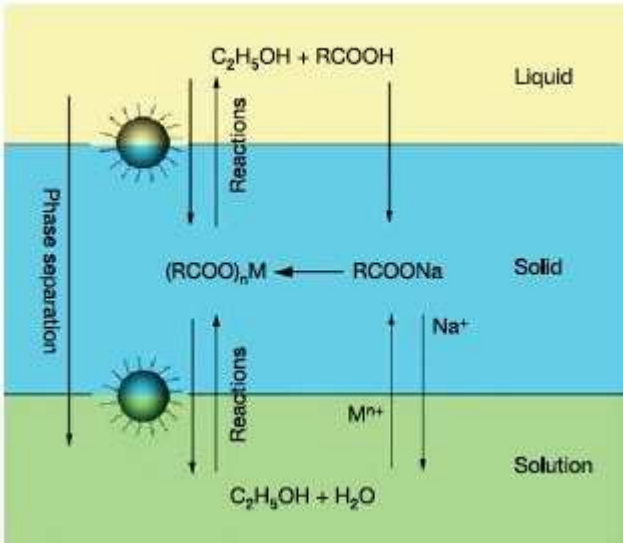

Fig. 7 Scheme of liquid–solid–solution (LSS) phase transfer synthetic Strategy. Adapted from ref 95. Copyright 2005, Nature Publishing Group

3.2.3. Hydrophilic ligand assisted hydro(solvo)thermal synthesis

Water soluble UCNPs can be prepared using hydrophilic ligands such as citrate (Cit^{3-}), [109-112] ethylenediaminetetraacetic acid (EDTA),[113,114] polyvinyl pyrrolidone (PVP),[115] cetyltrimethylammonuim bromide (CTAB),[116] poly(ethyleneimine) (PEI),[117-120] poly(acrylic acid) (PAA).[121,122] Polydentate Cit^{3-} is considered as one of the most important chelating and structure directing agent in upconversion phosphor synthesis. Lin and co-workers systematically studied the effect of various factors such as the amount of Cit^{3-}, pH value, and fluoride source in tailoring the crystal phases, shapes, and sizes of $NaREF_4$ (RE = Y, Yb, Gd, and Lu) nano/ microcrystals.[109-111] The products obtained using Cit^{3-} are often plate like microcrystals. EDTA and Na_2EDTA (Na_2EDTA, ethylenediamine tetraacetic acid disodium) are other polydentate organic additives which have similar structure-directing function as Cit^{3-}. Recently, Qiu et al. synthesized Yb and Er doped $BaYF_5$ nanoparticles using EDTA in a hydrothermal method.[114] They showed that the size of the $BaYF_5$ nanocrystals, can be controlled by the slow release of Ba^{2+} from chelating complex Ba-EDTA and reducing the pH levels. Apart from Cit^{3-} and EDTA, polymeric organic compounds with -NH_2 and -COOH groups also used to synthesis water soluble UCNPs. Wang et al. first reported the synthesis of PEI coated $NaYF_4$:Yb,Er/Tm NPs with an average particle size of 50 nm in ethanol solution. They also demonstrated that the high molecular weight of PEI is more efficient to control the particle growth and stabilize the particles against aggregation.[117] Later, they prepared monodisperse $NaYF_4$:Yb,Er/Tm nanoparticles of size 20 nm in ethylene glycol medium.[118] Li and co-workers reported the synthesis of β-$NaYF_4$:Yb,Er/Tm nanorods using PAA as surfactant in a facile solvothermal method.[121]

3.3. Other methods

In addition to those widely used methods, there are many other methods, such as co-precipitation, microwave assisted method, and ionic-liquids-based synthesis, which possess attractive advantages and have been employed to produce UCNPs.

3.3.1. Co-precipitation

Co-precipitation is one of the earliest and most convenient techniques for synthesizing UCNPs. Sub-10 nm REF_3 (RE = Eu, Er, Nd, Ho) NPs were prepared van Veggel and co-workers, through the co-precipitation of RE^{3+} and F^- ions assisted by ammonium di-n-octadecyldithiophosphate in ethanol-water solution at a low temperature of 75 °C.[135] Yi et al. synthesized $NaYF_4$:Yb,Er NPs by co-precipitation method in the presence of EDTA.[136] They controlled the particles size in the range of 37 to 166 nm by changing the molar ratio of EDTA to RE^{3+} ions. The as-prepared nanoparticles emit very weak upconversion fluorescence; however, when annealed at temperatures between 400 to 600 °C the emission intensities were enhanced by 40 fold. This is attributed the to the phase transition from cubic to hexagonal. Unfortunately, the NPs lost their spherical shape and aggregated after heating. Recently, He et al. synthesized Yb^{3+} and Er^{3+}/Tm^{3+}/Ho^{3+} co-doped β-$NaGdF_4$ microstructures in the presence of Na_2EDTA, PVP, sodium dodecyl sulfonate (SDS), and sodium tartrate (Na_2tar).[137] In their method, the surfactants play an important role in controlling the size, morphology, upconversion luminescence and magnetic properties of the microstructures. Even though, co-precipitation method is simple, post-heat treatment (annealing) is often required to promote UC fluorescent intensity which in turn allows the NPs to aggregate and become larger. After annealing, organic capping reagents such as EDTA and PVP will be carbonized, which reduces the hydrophilicity of the products.

3.3.2. Microwave-assisted synthesis

In the last few years, microwave-assisted method has aroused considerable attention in synthesis of UCNPs. Microwave heating offers many advantages over conventional heating such as higher heating rates, uniform heating throughout the sample, reduced reaction times, reduction in unwanted side reaction, higher yields and improved reproducibility.[141] Wang et al. synthesised oleic acid capped cubic $NaYF_4$ and $Na_xLi_yYF_4$ nanocrystals by facile microwave irradiation method. In this method the reaction time was significantly reduced to 5 min and synthesized nanoparticles were monodisperse and highly luminescent.[142] Mi et al. prepared highly crystalline, strongly luminescent $NaYF_4$:Yb,Er UCNPs in ethylene glycol at a lower temperature (160 °C) and shortened reaction time (only 1 h).[143] However, the crystalline phase of the as-prepared nanoparticles were mixture of both the α and β. Later, Yang and co-workers investigated the effect of various reaction parameters on the formation of phase pure $NaYF_4$:Yb,Er.[144] They demonstrated that increasing the NH_4F content in the ethylene glycol (EG) solvent, the phase of as-prepared nanoparticles can be gradually transformed from cubic to hexagonal.

3.3.3. Ionic liquids assisted synthesis

In recent years, ionic liquids have emerged as one of the most promising categories of medium for the synthesis of nanomaterials due to their exceptional features, such negligible vapour pressure, good thermal and chemical stability, relatively low viscosity, extremely high ionic conductivity, wide electrochemical windows.[147,148] In addition, ionic liquids have superior capability for the dissolution and stabilization of metal cations, which enables them with the possibility of acting as solvents, capping agents, or surfactants in inorganic synthesis. Zhang and co-workers reported the ionothermal synthesis of $NaYF_4$:Yb,Er/Tm UCNPs using 1-butyl-3-methylimidazolium tetrafluoroborate, [Bmim][BF_4].[149] In this method, the ionic liquid [Bmim][BF_4] acts as both the solvent and F^- source as well as template, which facilitates the formation of small hexagonal phase products. Ionic liquids are excellent absorbers of microwaves, and hence used as solvent and F^- source in microwave heating method. This method significantly reduces the reaction (5–20 min) and produces highly crystallized products.[150]

3.3.4. Gas-phase synthesis methods

Glaspel et al. reported the synthesis of Y_2O_3 nanocrystals doped with Yb^{3+}, Er^{3+}, Ho^{3+} using vapor phase synthesis approach based on the laser vaporization/controlled condensation (LVCC) technique.[151] This method combines the features of pulsed laser vaporization of target materials with a controlled condensation process from the vapor phase. This method produces highly crystalline upconversion nanocrystals and therefore eliminates the post-annealing process typically required for some other methods. Gas-phase flame synthesis is another promising technique since it can produce high-purity nanocrystals with small primary sizes in a single-step process. Qin et al. synthesized Yb^{3+} and Er^{3+} doped Y_2O_3 nanoparticles in two different sizes (27 and 14 nm) by controlling the flame temperature.[152] Kong et al. reported the flame synthesis of Yb^{3+}/Er^{3+} co-doped into Y_2O_3, La_2O_3, and Gd_2O_3 nanoparticles using flame synthesis. The average sizes of the particles were around 50 nm.[153]

3.4. Upconversion photoluminescence measurements

A typical setup for upconversion photoluminescence measurement is shown in Fig. 8.[154] In this setup, a fiber-coupled 980-nm laser is used as the excitation source for the upconversion excitation. A laser adapted and a beam collimator are used to guide the laser into the sample holder. The upconversion emission spectrum is recorded using a monochromator equipped with a photon counting photomultiplier. The excitation and the detection chambers are operated using a 90° measurement geometry in order to avoid the entrance of the excitation laser into the detector.

The measurement of absolute quantum yield (QY) of upconversion phosphors has been a difficult task. Page et al. pioneered the determination of the absolute quantum yield of bulk UC phosphors. The calculated QY was 4% for green emission of Yb^{3+},Er^{3+} doped hexagonal $NaYF_4$.[155] van veggel et al. reported technique for measuring QYs of upconverting nanomaterials based on the use of a commercially available fluorimeter and an integrating sphere. By using this setup, they calculated the QY of colloidal β-$NaYF_4$:Yb^{3+},Er^{3+} nanoparticles. The values were in the range of 0.005% to 0.3%, depending on the particle size.[156]

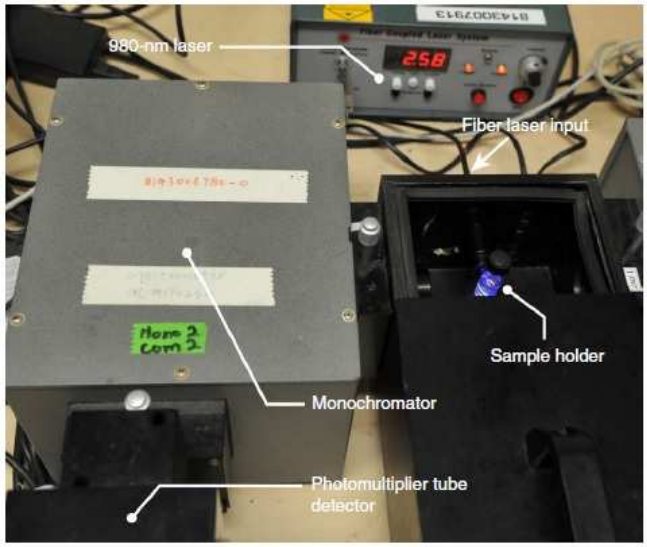

Fig. 8 Photograph of the experimental setup for the measurement of upconversion emission spectra. Adapted from ref 154. Copyright 2014, Nature Publishing Group.

4. Upconversion luminescence enhancement

The synthesis of highly luminescent UCNPs is very important in considering the application of these NPs in solar cells and other fields. There are several strategies available to enhance the upconversion luminescence such as (1) impurity doping (2) plasmonic enhancement and (3) construction of core-shell nanostructures.

4.1. Impurity doping

It is well known that upconversion luminescence intensities of lanthanide ions are mainly dependent on electronic transition probabilities, which is highly sensitive to the surrounding environment of the Ln^{3+} ions. Consequently, tailoring the local crystal field of the Ln^{3+} ions could be an effective strategy to increase the UC emissions for various host materials doped with lanthanide ions. The crystal symmetry in UC nanocrystals can be altered by an intentional doping of non luminescent cationic ions. Fig. 9 shows the possible changes in the crystal lattice after impurity doping. For homo-valance doping, depending on the size of the impurity dopants, the host lattice will contract (smaller dopants) or expand (larger dopants). Hetero-valence ion doping always accompanied by formation of vacancy sites or an extra ion occupying the interstitial site. In addition, it is also possible to dope the impurities directly into the interstitial positions.[157] One of the most successful impurity ion is Li^+, due to its small ionic radius, Li^+ ion can be doped easily into the host lattice substitutionally or interstitially. This will result in the alteration of crystal field around the rare-earth ions, leading to the enhanced upconversion PL intensity. Li^+ doping was found to be highly successful in oxide UCNPs of varying host lattice and lanthanide dopants.[158-160] For example, Zhang and co-workers, observed a 25 times enhancement

of the visible UC emissions in Li^+ co-doped Y_2O_3:Yb,Er NPs.[158] Recent reports show that the Li^+ doping can also produce the same

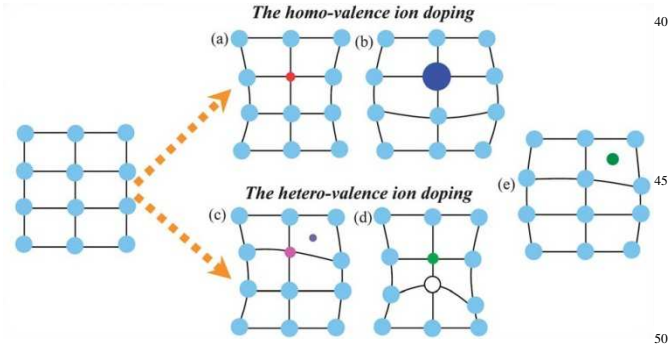

Fig. 9 Schematically illustrating the possible impurity doping routes in the host lattice: (a) substitution by a small homo-valence dopant, (b) substitution by a large homo-valence dopant, (c) combination of substitution by a hetero-valence dopant and interstitial occupation by an extra ion for charge compensation, (d) combination of substitution by a hetero-valence dopant and vacancy occupation for charge compensation, and (e) interstitial occupation by a small dopant. Adapted from ref 157. Copyright 2013, The Royal Society of Chemistry.

results in fluorides host materials such as $NaYF_4$:Yb,Er/Tm.[142,161-163] Besides Li^+, other cations such as Bi^{3+}, Fe^{3+}, Sc^{3+}, and Ca^{2+} can also be used to tailor the local crystal symmetry.[144,57,164,165] For example, Huang et al. observed enhanced upconversion emissions in hexagonal $NaYF_4$ by tridoping the structure with Sc^{3+},Er^{3+},Yb^{3+}.[164] They systematically studied the change in crystal symmetry of $NaYF_4$:Yb,Er by Sc^{3+} doping, using X-ray diffraction (XRD), X-ray photoelectron spectroscopy (XPS), and decay time investigations. Our group, recently observed fluorescence enhancement in Fe^{3+} doped $NaGdF_4$:Yb,Er nanocrystals.[57] In 30 mol% Fe^{3+} doped samples, the green and red UC emission were enhanced by 34 and 30 times, respectively (Fig. 10).

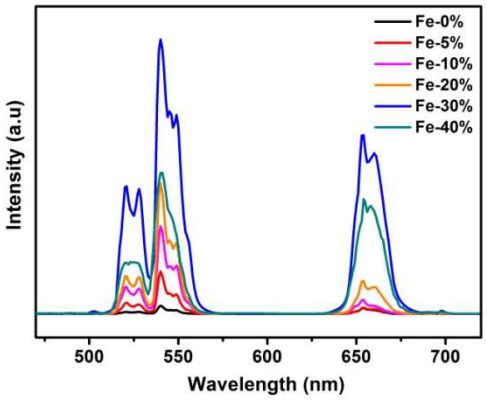

Fig. 10 UC luminescence spectra of $NaGdF_4$:Yb,Er,Fe (0–40 mol%) nanoparticles under 980 nm excitation at room temperature. Reproduced from Ref 57. Copyright 2013, The Royal Society of Chemistry.

4.2. Plasmonic enhancement

Localised surface plasmon resonance (LSPR) from noble metal nanostructures can be used to enhance the upconversion luminescence. There are three different methods usually followed to enhance the UC emission using plasmonic nanostructures. (1) Deposition of upconversion nanoparticles on metallic nanostructure films. UC nanoparticles have been deposited over a variety of metallic films such as gold islands,[166] dense metal nanoparticles (Ag or Au),[167,168] 3D plasmonic antenna,[169] Au nanohole arrays,[170] and gold pyramid arrays.[171] Zhang et al. observed five-fold overall enhancement of upconversion emission in $NaYF_4$:Yb,Er nanocrystals when coupled with gold island films.[166] The upconversion enhancement is highly depends on the distance between the upconverters and the metallic structures. Saboktakin et al. proposed a new configuration in which close-packed monolayers of UCNPs are separated from a dense multilayer of metal NPs (Au or Ag) by a nanometer-scale aluminium oxide grown by atomic layer deposition (Fig. 11). The spacer layer thickness was varied from 2 to 15 nm. They observed 45 fold enhancement for $NaYF_4$:Yb,Er nanoparticles over Ag nanoparticles films separated by 10 nm Al_2O_3 oxide.[168] Recently, the same group reported 35 fold enhancement in the upconversion luminescence of $NaYF_4$:Yb,Er in Au nanohole arrays.[170] The enhancements were mainly due to the combined effects of enhancement in the excitation of sensitizers and increase in radiative decay rate of emitters. (2) In the second approach metal nanoparticles or nanoshells are formed on the surface of UCNPs. Zhang et al. studied the effect of gold nanoparticles or nanoshells on the UC emission of $NaYF_4$:Yb,Tm hexagonal nanoplates.[172] Attachment of gold nanoparticles enhanced the upconversion by a factor of 2.5, whereas the growth of nanoshells quenched the UC emissions by a factor 3 to 4. Li et al. also observed the same phenomenon in $NaYF_4$:Yb,Er,Gd nanorods.[173] It was proposed that the gold shell on the UCNPs can significantly scatter the excitation light at 980 nm and reduces the excitation flux. In addition, the complete surrounding gold shell can also block the emission transmittance from the UCNPs. (3) The third is by forming core-shell structure of metal NPs-silica-UCNPs or UCNPs-silica-metal NPs. This method allows one to precisely control the distance between UCNPs and metal NPs. Various core-shell structures such as $NaYF_4$:Yb,Er@SiO_2@Ag, $NaYF_4$:Yb,Er@SiO_2@Au, and Ag@SiO_2@Y_2O_3:Er have been developed to enhance the UC luminescence.[174-176] Yuan et al. observed 14.4 fold enhancement in $NaYF_4$:Yb,Er@SiO_2@Ag core-shell nanostructures with 10 nm SiO_2 shell thickness. They also found that the use of different size Ag NPs resulted in different enhancement factor (14.4 times for 15nm and 9.5 times for 30 nm Ag NPs).[174]

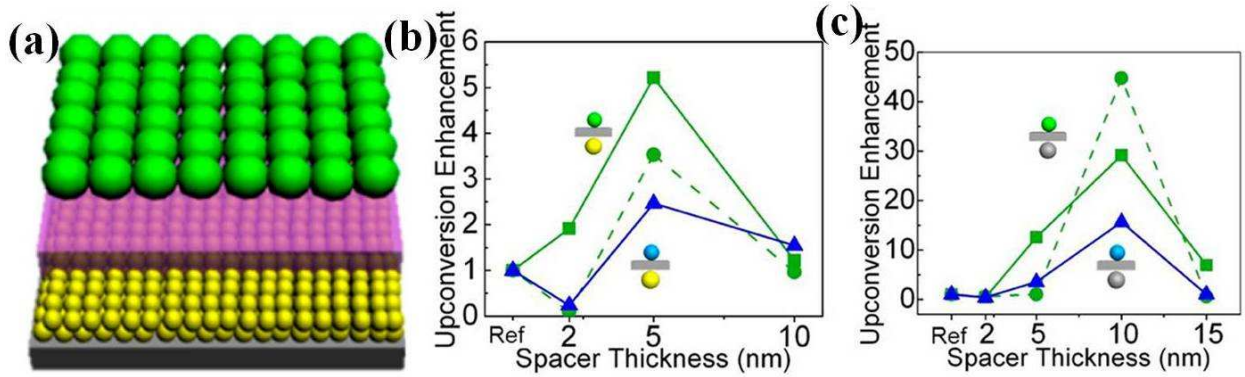

Fig. 11 (a) Schematic structure of a spin-cast layer of Au or Ag NPs, a thin Al_2O_3 layer, and a monolayer of UCNPs. Integrated area under the upconversion emission peak as a function of the Al_2O_3 layer thickness normalized to that of the pure UCNP sample for (b) Au NPs and (c) Ag NPs. The green solid lines correspond to the 540 nm emission band (510-570 nm) in $NaYF_4$:Yb, Er. The green dashed lines correspond to the 650 nm emission band (640-680 nm) in $NaYF_4$:Yb,Er. The blue solid lines correspond to the 475 nm emission band (461-490 nm) in $NaYF_4$:Yb,Tm. Reprinted with permission from Ref 168. Copyright 2012, American Chemical Society.

4.3. Core-shell nanostructures

Construction of core-shell structures has become an important strategy in UC nanomaterials synthesis to improve the emission of UCNPs. The shell enhances the photoluminescence by protecting the luminescent ions in the core from non-radiative decay caused by the surface defects as well as from vibrational deactivation ascribed to solvent molecules and ligands absorbed on the NCs surface. Commonly, the core-shell structures can be classified into two types. In type 1, the active Ln^{3+} doped core is covered with an undoped inert shell such as, $NaYF_4$:Yb,Er@$NaYF_4$ and $NaYF_4$:Yb,Er@$NaGdF_4$.[61-71] Yi et al. reported that the visible UC emissions in hexagonal phase $NaYF_4$:Yb,Er and $NaYF_4$:Yb,Tm were enhanced by 7.4 times and 29.6 times, respectively, by growth of a thin layer of $NaYF_4$ (~2 nm).[177] Besides rare-earth fluoride shells, CaF_2 have also explored as an efficient heterogeneous shell material to enhance the upconversion emission. Wang et al. reported ~300 fold enhancement of UC emission yield in the 10-13 nm $NaYF_4$:Yb,Er@CaF_2 core-shell nanoparticles in comparison to the core $NaYF_4$:Yb,Er nanoparticles.[178] In the second type of core-shell structures, the shell material also doped with lanthanide ions (Fig. 12a). In this type, the Ln^{3+} ions in the shell further enhances the UC emission by interacting with the Ln^{3+} dopants in the core nanoparticles. Capobianco et al. reported the synthesis of $NaGdF_4$:Yb,Er active-core@$NaGdF_4$:Yb active shell nanoparticles and observed enhanced upconversion emission compared to either the $NaGdF_4$:Yb,Er active-core@$NaGdF_4$ inert shell or the $NaGdF_4$:Yb,Er core-only nanoparticles.[179] The Yb^{3+} ions in the active shell can harvest more NIR light and transfer the core. Wang *et al.* synthesized a series of $NaGdF_4$:Yb,Tm@$NaGdF_4$:Ln (Ln = Eu, Tb, Dy, Sm) NPs. They realized tunable UC emissions for Eu^{3+}, Tb^{3+}, Dy^{3+}, and Sm^{3+} ions by taking advantage of energy transfer processes from sensitizer Yb^{3+} to accumulator Tm^{3+}, then to migrator Gd^{3+}, and finally to activator Ln^{3+} ions. Making use of this structure, the colour of Eu^{3+} doped samples can be tuned from blue to red by changing the Eu^{3+} concentration from 0 to 15 mol % in shell.[180]

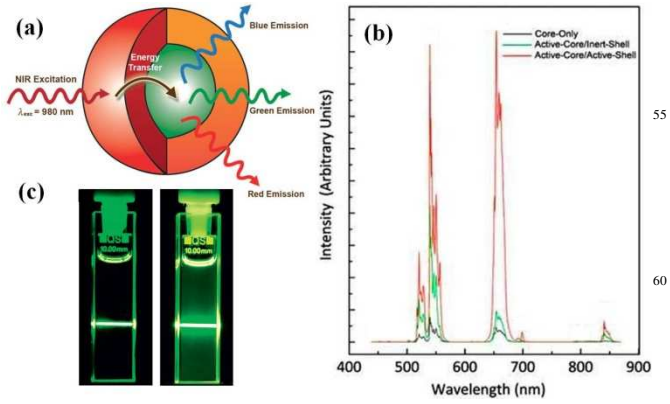

Fig. 12 (a) General depiction of the active-core/active-shell nanoparticle architecture showing the absorption of NIR light by the Yb^{3+}-rich shell (represented in red) and subsequent energy transfer to the Yb,Er co-doped core (represented in green), which leads to upconverted blue, green, and red emissions. (b) Upconversion luminescence spectra of colloidal core-shell nanoparticles. (c) Photographs of colloidal solutions of (A) $NaGdF_4$:Yb,Er active-core/$NaGdF_4$ inert-shell nanoparticles and (B) active-core/active-shell $NaGdF_4$:Yb,Er/$NaGdF_4$:Yb nanoparticles in toluene (1 wt%) following excitation with 980nm. Reprinted with permission from Ref 179. Copyright 2009, WILEY-VCH Verlag GmbH & Co. KGaA, Weinheim.

5. Solar cell application

Gibart *et al.* first reported the application of upconversion phosphors for improving the performance of solar cells in 1996. They combined the GaAs solar cell with a vitroceramic material doped with Yb^{3+} and Er^{3+}, and obtained an efficiency of 2.5% under high excitation densities.[181] Since then, many research groups have involved in the development of upconversion based

solar cells. Upconversion materials singly doped with Er^{3+} or Ho^{3+}, are highly suitable for narrow bandgap c-Si solar cells (Eg = 1.12 eV; 1100 nm), since they can convert long-wavelength (~ 1500 nm) NIR light into short-wavelength (980 800, 660, 550 nm) NIR and visible emissions. For other solar cell types such as amorphous Silicon (a-Si), DSSC, and organic solar cells, the utilization of Yb^{3+} co-doped with Er^{3+} or Ho^{3+} upconversion materials is very convenient due to efficient ETU from the Yb^{3+} sensitizer to the activators.

5.1. Upconversion for c-Si solar cells

Er^{3+} doped upconversion materials are widely used for c-Si solar cells due to the GSA of Er^{3+} in the range of 1480–1580 nm ($^4I_{15/2}$ - $^4I_{13/2}$ transition). When absorb a certain number of photons with wavelength of about 1500 nm, Er^{3+} ion produces four upconversion emission bands: $^4I_{11/2}$- $^4I_{15/2}$, 980 nm; $^4I_{9/2}$-$^4I_{15/2}$, 810 nm; $^4F_{9/2}$-$^4I_{15/2}$, 660 nm; and $^4S_{3/2}$-$^4I_{15/2}$, 550 nm (Fig. 13).[176] These emission bands are well matched with the absorption region of c-Si. Shalav et al.[65] used Er^{3+} doped $NaYF_4$ upconversion phosphor to enhance the responsivity of silicon solar cell in the NIR. The phosphors were mixed into an optically transparent acrylic adhesive medium and attached to the rear side of a bifacial silicon solar cell. An external quantum efficiency of 2.5% was obtained for the solar cell under excitation at 1523 nm with a 5.1 mW laser.[182] Fisher and co-workers, also investigated the application of Er^{3+} doped $NaYF_4$ to enhance the conversion efficiency of c-Si solar cells. The UC efficiency of $NaYF_4$:Er^{3+} phosphor was determined to be 5.1% at a monochromatic irradiance of 1880 W m^{-2} at 1523 nm. The c-Si solar cell with the upconvertion phosphor produced an external quantum efficiency of 0.34% at an irradiance of 1090 W m^{-2} at 1522 nm.[183] Liang et al. proposed $Gd_2(MoO_4)_3$:Er^{3+} nanophosphors as potential luminescent materials to enhance the response of the silicon solar-cell in NIR region. Upon excitation with low-energy near-infrared photons, the phosphor produced intense upconverted emissions at 545, 665, 800, and 980 nm, with an efficiencies of 0.12%, 0.05%, 0.83%, and 1.35%, respectively.[185] Recently, Meijerink and co-workers, investigated the luminescence properties of Er^{3+}-doped Gd_2O_2S for solar cell application. UC emission and quantum yield measurements showed that Gd_2O_2S doped with 10% Er^{3+} has an internal UC quantum yield of 12.0 ± 1.0% under monochromatic excitation around 1500 nm at a power of 700 W/m^2. This value is higher than the well-known Er^{3+}-doped β-$NaYF_4$ (8.9 ± 0.7%).[188]

Besides Er^{3+} ion, Ho^{3+} doped UC phosphors also explored to enhance the performance of c-Si solar cells. Lahoz in 2008, used Ho^{3+} doped oxyfluoride glass ceramics as promising upconverters for efficiency enhancement in c-Si solar cells. The Ho^{3+} ion has a relatively wide absorption band in the 1150-1225 nm spectral range due to $^5I_8$-$^5I_6$ transition. When exited under 1170 nm, the Ho^{3+} ion emits two upconverted emissions in the visible (~650 nm, $^5F_5$-$^5I_8$ transition) and NIR (~910 nm, $^5I_5$ - $^5I_8$ transition) spectral ranges *via* ETU mechanism.[192] Later, Lahoz et al. co-doped Ho^{3+} with Yb^{3+} in fluoroindate glass and observed enhanced upconversion efficiency as a function of Yb^{3+} concentration. Because of the high transparency around 1540 nm of Ho^{3+} doped phosphors, the authors proposed a double-layer structure of Ho^{3+} doped material together with Er^{3+} doped material to take advantage of the UC potential of both types of materials.[193]

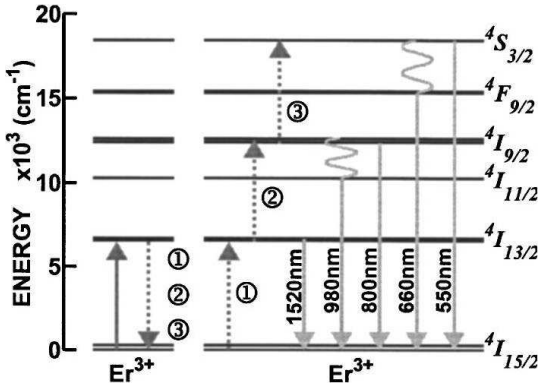

Fig. 13 Three-step UC process between two erbium Er3+ ions. Energy relaxation from one Er^{3+} ion (the sensitizer) can result in energy transfer to a neighboring Er^{3+} ion (activator) giving rise to higher energy photons. Solid lines represent photon absorption (up) and emission (down), dotted lines represent energy transfer, wavy lines represent phonon emission. For the two step process, photons with energies greater than the band gap of silicon are emitted. Reproduced with permission from Ref 182. Copyright 2005, American Institute of Physics.

Because of the high transparency around 1540 nm of Ho^{3+} doped phosphors, the authors proposed a double-layer structure of Ho^{3+} doped material together with Er^{3+} doped material to take advantage of the UC potential of both types of materials.[193] Recently, Cheng et al. proposed a core-shell structure to extend the NIR wavelength range excitable for upconversion emission. The authors synthesized $NaGdF_4$:Er^{3+}@$NaGdF_4$:Ho^{3+}@$NaGdF_4$ core-shell-shell nanoparticles and investigated their upconversion properties. In these NCs, the intermediate shell enhances the UC luminescence of Er^{3+} in the core by passivation mechanism and as well as act as the host to realize the UC luminescence of Ho^{3+}. More importantly, the upconversion quenching of Er^{3+} and Ho^{3+} was effectively suppressed by doping Er^{3+} and Ho^{3+} in the nanoparticles core and shell, respectively. As a result, intense upconversion emissions for both Er^{3+} and Ho^{3+} dopants were achieved.[194]

5.2. Upconversion for amorphous silicon solar cells

Compared with crystalline silicon, amorphous silicon has a band gap of ~1.75 eV, can only absorb light shorter than 708 nm. In order to utilize the NIR light in amorphous Si solar cells, Yb^{3+} co-doped with Er^{3+} or Ho^{3+} upconversion materials can be used. Zhang and co-workers, synthesized $NaYF_4$:Yb,Er nanoparticles using EDTA assisted hydrothermal method. Upconverter layer was fabricated by mixing the phosphor with polydimethylsiloxane (PDMS), and attached to the rear side of the solar cell. The short circuit current density of the device was increased from 15.99 to 17 mA/cm^2.[195] Wild et al. mixed the upconversion $NaYF_4$:Yb,Er phosphor with polymethylmethacrylate and then made into an

upconverter layer with thickness of 200-300 mm. A maximum current enhancement of 10 μA was measured on illumination with a 980 nm diode laser at 10 mW.[196,197] Li et al. prepared gold nanostructures decorated $NaYF_4$:Yb,Er,Gd nanorods and applied in a-Si solar cells. The authors obtained 72-fold improvement of the short-circuit current and maximum current of 1.16 mA for the cell using UC nanorods coated with Au nanoparticles under 980 nm laser illumination.[198] Recently, Wild et al. showed the upconversion photoresponse in a-Si solar cells with broad-band light excitation using Gd_2O_2S: Yb^{3+},Er^{3+} upconverter. The authors made a set-up to concentrate near infrared light (longer than 900 nm) from a solar simulator up to 25 times. The photo response obtained from broadband excitation was the same as that under laser light excitation.[201]

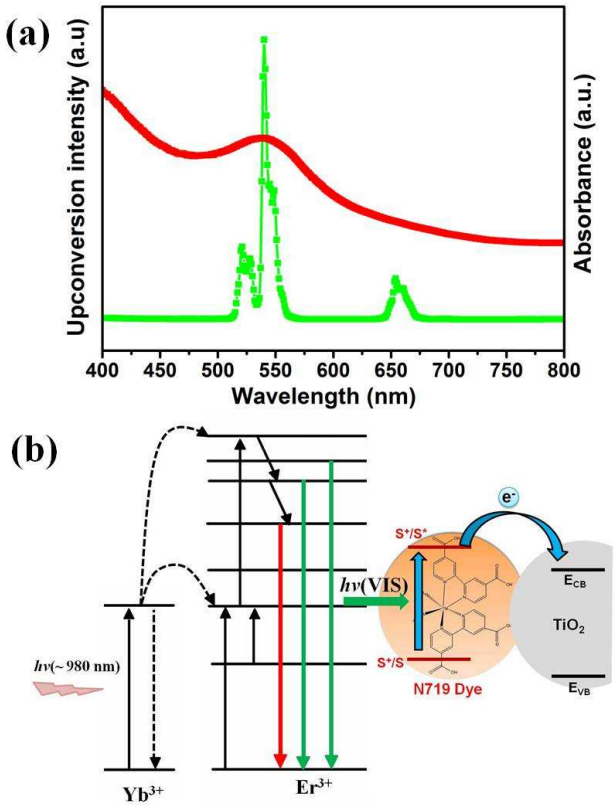

Fig. 14 (a) Absorption spectrum of N719 dye and UC photoluminescence spectrum of $NaYF_4$:Yb,Er nanoparticles. (b) Energy level diagram of upconversion DSSC shows the energy transfer from UC nanocrystals to the N719 dye.

5.3. Upconversion for Dye-sensitized solar cells

Dye-sensitized solar cells have attracted increasing attention in the solar energy conversion sector due to their low cost, easy fabrication, and high efficiencies. Unlike Si solar cells, typical DSSC consists of a dye-sensitized nanocrystalline TiO_2 semiconductor film on transparent conductive oxide (TCO) glass, an electrolyte solution containing a $I^-/I3^-$ redox couple, and a platinum coated TCO glass as a counter electrode. Upon excitation, the dye molecules absorb photons and inject electrons into the conduction band of TiO_2 from the excited state of the dye. The dye ground state is regenerated by electron transfer from a redox species in solution, which is then reduced at the counter electrode. By great efforts of the researchers, DSSCs have reached an efficiency of 13%.[202] However, this conversion efficiency is still not enough for commercialization. A major factor limiting the performance of DSSCs is the incapacity of utilizing the near-infrared (NIR) and infrared photons (IR) photons. The most commonly used sensitizers such as N3, N-719, and N-749 can absorb light with wavelengths in a range between 300 and 800 nm due to their large bandgap ~ 1.8 eV.[203,204] DSSCs can effectively utilize the NIR light by the aid of upconversion emission from UCNPs. Fig. 14 shows the absorption spectrum of N719 dye and UC emission spectrum of β-$NaYF_4$:Yb,Er nanoparticles. The absorption peak of N719 dye is well resonance with green emission (~550 nm) of the UCNPs. As a consequence, the NIR light absorbed by the UCNPs can be effectively used to excite the dye molecules (Fig. 14b), which in turn will help to increase the performance of DSSCs in NIR region.

In 2010, Shan and Demopoulos reported, for the first time application of UCNPs for enhancing the NIR sunlight harvesting in DSSCs.[205] In their studies, they prepared Yb^{3+} and Er^{3+}co-doped LaF_3-TiO_2 nanocomposites and used as an upconversion layer to fabricate a triple-layer working electrode for DSSCs. The green emission from the upconversion nanocomposite can be efficiently absorbed by the N719 dye, and generates the photocurrent upon 980 nm laser excitation. However, this structure was ineffective and the overall efficiency of the DSSCs decreased due to apparent charge recombination at the UCNP/dye/electrolyte interfaces. Later, several research groups have successfully modified this strategy to improve the performance of DSSCs.[206-225] For example, Wu et al. reported the enhanced photovoltaic performances of DSSCs by doping $Y_{0.78}Yb_{0.20}Er_{0.02}F_3$ in TiO_2 photoanode. The DSSC with 7 wt% $Y_{0.78}Yb_{0.2}Er_{0.02}F_3/TiO_2$ in the doping layer exhibited higher short-circuit current density (J_{SC} = 15.58 mA cm^{-2}), open-circuit voltage (V_{OC} = 0.80 V), and a power conversion efficiency (η) of 7.90%, which is significantly higher than the DSSC without REF_3 doped TiO_2 layer (J_{SC} = 13.33, V_{OC} = 0.73, and η = 5.84%). The enhanced J_{SC} mainly come from the upconversion luminescence of Yb^{3+}/Er^{3+}, which results in more incident light harvesting. On the other hand, doping REF_3 in TiO_2, gives p-type doping effect, which elevates the flat-band potential and the Fermi level of the TiO_2 electrode, thus increases the V_{OC}.[206]

Table 2. Selected lanthanide-doped upconversion materials used for solar cell applications

Dopant ion	Host lattice	Excitation (nm)	Emission (nm)	Solar cell type	Ref
Er^{3+}	$NaYF_4$	1523	550, 660, 800, 980	c-Si	182,183
Er^{3+}	CaF_2	1550	660, 980	c-Si	184
Er^{3+}	$Gd_2(MoO_4)_3$	1530	545, 665, 800, 980	c-Si	185
Er^{3+}	$NaGdF_4$	1530	527, 540, 653	c-Si	186
Er^{3+}	Y_2O_3	1538	562, 659, 801, 987	c-Si	187
Er^{3+}	Gd_2O_2S	1510	540, 660, 820, 990	c-Si	188
Er^{3+}	Fluoride glass	1532	550, 660, 820, 980	c-Si	189
Er^{3+}	BaY_2F_8	1557	540, 670, 800, 970	c-Si	190
Yb^{3+}, Er^{3+}, In^{3+}	$LiNbO_3$	1550/980	530, 558, 672	c-Si/a-Si	191
Ho^{3+}	Glass ceramics containing PbF_2 nanocrystals	1170	650, 910	c-Si	192
Yb^{3+}, Ho^{3+}	Fluoroindate glass	1155	550, 650, 750, 905, 980	c-Si	193
Yb^{3+}, Er^{3+}	$NaYF_4$	980	525, 540, 640-660	a-Si	195-197
$Yb_{3+,}$ Er^{3+},Gd^{3+}	$NaYF_4$	980	540, 660	a-Si	198
Yb^{3+}, Er^{3+}	Glass ceramic containing $NaYF_4$ nanocrystals	980	520, 538, 656	a-Si	199
Er^{3+}	$NaYF_4$	1560,980	540, 650, 803, 980	a-Si	200
Yb^{3+}, Er^{3+}	Gd_2O_2S	980	510-560, 650-680	a-Si	201
Yb^{3+}, Er^{3+}	LaF_3	980	543, 655	DSSC	205
Yb^{3+}, Er^{3+}	YF_3	980	525, 545, 656	DSSC	206
Yb^{3+}, Er^{3+}	$NaYF_4$	980	520- 570, 650-700	DSSC	207-217
Yb^{3+}, Er^{3+}, Fe^{3+}	$NaGdF_4$	980	525, 540, 653	DSSC	218
Yb^{3+}, Er^{3+}	$Na(Y_{1.5}Na_{0.5})F_6$	980	540, 660	DSSC	219
Er^{3+}	Y_2O_3	980	560, 660	DSSC	220
Yb^{3+}, Er^{3+}	Gd_2O_3	980	564, 650-700	DSSC	221
Yb^{3+}, Er^{3+}	$Y_3Al_5O_{12}$	980	563, 677	DSSC	222
Yb^{3+}, Er^{3+}	TiO_2	980	533, 547, 658	DSSC	223,224
Er^{3+}	TiO_2	980	439, 488, 536, 565, 664	DSSC	225
Yb^{3+},Tm^{3+}	Lu_2O_3	980	476, 653	DSSC	226
Yb^{3+}, Er^{3+}	YF_3	975	540, 660	Organic	227
Yb^{3+}, Er^{3+}	MoO_3	975	520-540	Organic	228
Yb^{3+}, Er^{3+}	$NaYF_4$	980	540, 660	Organic	229,231
Yb^{3+}, Ho^{3+}	Y_2BaZnO_5	986	545, 660, 780	Organic	230

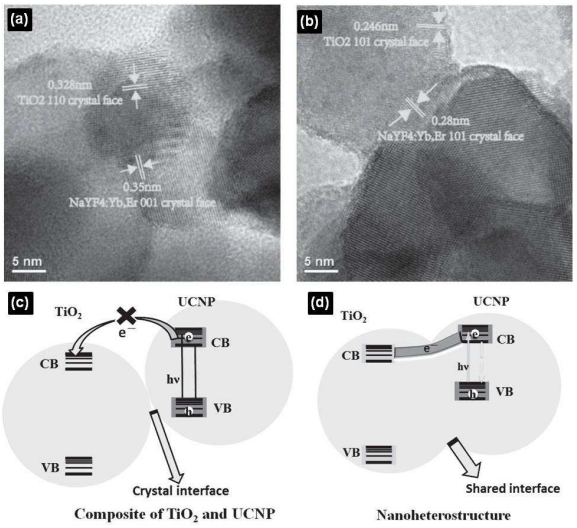

Fig. 15 HR-TEM images of TiO_2/UCNP nanocomposites sintered at (a) 400 °C and (b) 450 °C. Schematic representation of the (c) composite and (d) nano-heterostructure of TiO_2 and UCNPs. CB = conduction band. VB = valence band. Reprinted with permission from 201. Copyright 2013, WILEY-VCH Verlag GmbH & Co. KGaA, Weinheim.

Chang et al. observed an enhanced efficiency in DSSCs with in situ prepared TiO_2/$NaYF_4$:Yb^{3+}, Er^{3+} nano-heterostructures on the TiO_2 photoanode of DSSC.[207] The TiO_2 photoanodes were prepared by mixing different amounts of UCNPs with TiO_2 NPs and screen printing on the FTO glass, followed by heat treatment at 400 or 450 °C. In 450 °C sintered samples some of the crystal phases between TiO_2 and the UCNPs disappeared and shared interfaces (nano-heterostructures) were formed, whereas in 400 °C sintered samples, UCNPs and TiO_2 had clear interfaces and no nano-heterostructures were formed (Fig. 15). They found that the formation of nano-heterostructures between TiO_2 and UCNPs, facilitates the effective electron injection from the UCNPs to the conduction band (CB) of TiO_2, which is not possible in physically mixed samples. The DSSCs using the photoanodes containing the nano-heterostructure produced 17% higher efficiency than that of the device without UCNPs and 13% higher than that of the device containing physically mixed TiO_2 and UCNPs, which clearly highlights the effect of the direct electron injection from UCNPs to the CB of TiO_2. Zhao and co-workers, used new scattering and upconverting layer composed of double shell β-$NaYF_4$:Yb,Er/SiO_2/TiO_2 submicroplates on top of the transparent TiO_2 layer for DSSCs.[215,216] The β-$NaYF_4$:Yb,Er cores can harvest the NIR light and re-emit visible upconversion light, which broadens the absorption spectrum of DSSC and more photoinduced electrons can be produced to enhance the photocurrent. The thin SiO_2 inner shell can act as an insulating layer to separate the upconversion cores from the external environment and the recombination effect can be completely eliminated. The dye loading ability was enhanced by the outer nanoporous TiO_2 shells. In addition, owing to the submicron dimensions, these microplates can act as effective Mie scatterers, leading to a significant enhancement of the light harvesting capability. DSSC employing β-$NaYF_4$:Yb,Er/SiO_2/TiO_2 submicroplates top layer exhibited 29.41% improvement in the energy conversion efficiency (7.70%) compared with the cell composed of the nanocrystalline TiO_2 film (5.95%).[215] In a recent report, Wang and co-workers synthesized upconversion Yb^{3+} and Er^{3+} doped TiO_2 nanoshells and applied to improve the performance of DSSCs. The upconverters doped TiO_2 nanoshell acted as both the light scattering layer as well as NIR harvesting layer. An overall conversion efficiency of 9.12% was achieved with this dual-functional UC-TiO_2 hollow shells, corresponding to ~ 32.7% enhancement compared with the 6.87% efficiency for a P25 photoanode.[223]

Shan et al. proposed a new DSSC structure, in which the upconverting $NaYF_4$:Yb,Er microplates were placed on the rear side of the counter electrode.[212] This design enables a dual-mode functionality that provides both light reflection and NIR light harvesting. Under AM 1.5G filtered spectral illumination (100 mW cm-2) approximately 10% enhancement in conversion efficiency was achieved. The observed enhancements was predominantly due to the light reflecting action of the β-$NaYF_4$:Yb,Er. The upconversion contribution from the Er^{3+},Yb^{3+} dopants was very low (~1%) and the authors concluded that more efficient UCNPs need to be developed to render up-conversion a viable option in solar cell fabrication. Recently, our group developed a new strategy to improve the efficiency of DSSCs by using external NIR light harvesting and light-reflecting bifunctional layers consisting of upconversion nanoparticles combined with silver particles.[218] We used 30 mol% Fe^{3+} doped β-$NaGdF_4$:Yb,Er UCNPs, which have 30 times more upconversion luminescence than the undoped UCNPs. The enhanced upconversion luminescence in Fe^{3+} doped UCNPs can be more beneficial for solar cell applications. The schematic diagram of the DSSC structure is shown in Fig. 16. The rear reflector layer was fabricated on a microscopic glass slide by drop casting 50 µL of silver particles followed by drying at 70 °C. Upconversion nanoparticles layer was coated by dropping 50 µL of UCNPs (1 wt% in toluene) and dried at 80 °C for 2 min. Rear reflector films were attached to the counter electrode using scotch tape or sealant (Surlyn, 60 µm-thick, Meltonix). The UCNPs can harvest the NIR light and emit visible photons. Silver particles can function as a back reflector for the upconverted visible photons emitted from the UCNPs bouncing back into the DSSC. In addition we found that silver particles further enhanced the upconversion luminescence by the plasmonic effect. The DSSC with a plasmonic and upconversion rear reflector achieved a conversion efficiency of 7.04% under one sun illumination, which is an increase of 21.3% compared to the cell without a rear reflector (5.8%).[218]

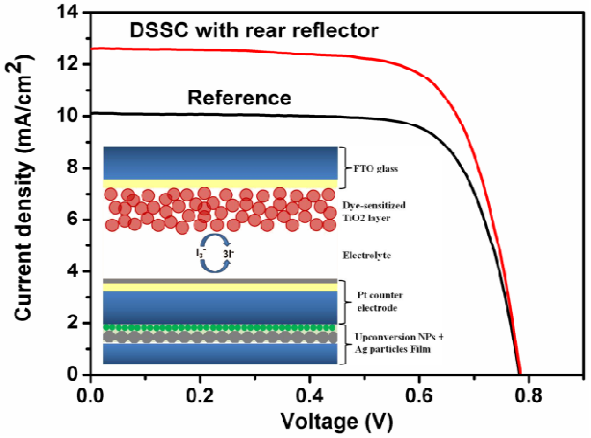

Fig. 16 J-V curves of the DSSCs with and without rear reflector films. Inset shows the schematic diagram of the DSSC with rear reflector film.

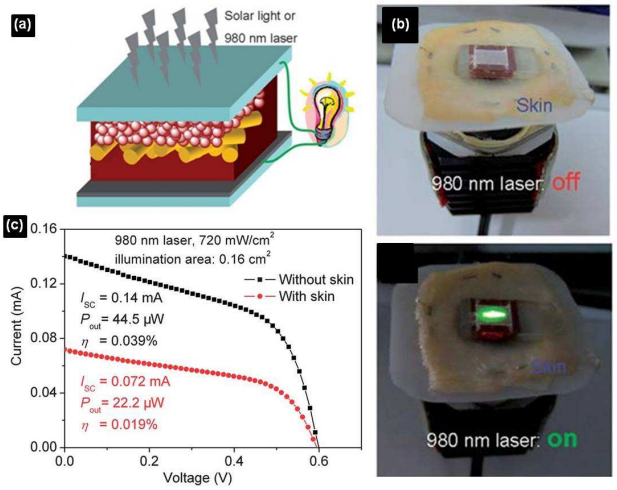

Fig. 17 (a) schematic illustration of 980LD-PVCs containing $NaYF_4$:Yb,Er nanorod film. (b) Photos of TCO glass/N3-sensitized TiO_2 film/$NaYF_4$:Yb,Er film on the skin with the support, when 980 nm laser turns off and on. (c) Photocurrent–voltage characteristics of 980LD-PVC covered without and with chicken skin under the irradiation of a 980 nm laser with an intensity of 720 mW cm^{-2}. Reproduced from Ref 205. Copyright 2012, The Royal Society of Chemistry.

Chen and co-workers, demonstrated the potential application of UCNPs to construct implantable DSSCs to power next generation in vivo devices.[211] The authors prepared 980 nm laser-driven photovoltaic cell (980LD-PVC) introducing a $NaYF_4$:Yb,Er nanophosphor layer in conventional DSSC (Fig. 17). An ethanol dispersion of 1 mg/mL $NaYF_4$:Yb,Er nanorods was drop casted on the N3 dye-sensitized TiO_2 film, followed by heating at 40 °C in air for 30 min to remove the ethanol. This casting process was repeated until a 4 µm thick $NaYF_4$:Yb,Er nanorod film was prepared. They further replaced the conventional liquid electrolyte with highly thermostable succinonitrile-based gel electrolyte to avoid any leakage and evaporation of the solvent. Under the irradiation of 980-nm laser with a power of 720 mW cm^{-2}, the 980LD-PVC produced a output power of 44.5 µW and an overall conversion efficiency of 0.039%. More importantly, after being covered with chicken skin (thickness: 1 mm) as a model of biological tissue, 980LD-PVC still possesses a maximum output power of 22.2 µW and an overall conversion efficiency of 0.019%. This output power (22.2 µW) is excellent enough to satisfy the power requirements of many biological devices, such as in vivo nanorobots (at least 1 µW) and cardiac pacemakers (about 10 µW). Although there are some biologically non-compatible components (such as the glass electrode) are present in 980LD-PVCs, they can be potentially replaced by other biocompatible components such as a flexible plastic electrode.

5.4. Upconversion for organic solar cells

Organic solar cells are considered as one of the promising candidates for low cost photovoltaic because of their obvious advantages such as light weight, simple fabrication, flexible and low cost. The best performing organic solar cells are made of bulk heterojunctions comprising of donor poly(3-hexylthiophene) (P3HT) and the acceptor fullerene derivative [6,6]-phenyl-C61-butyric acid methyl ester (PCBM). Upon excitation, the donor material absorbs the light and produces excitons, which are then transported to the donor/acceptor interface. From there, the electrons that exist in a higher energy state are transferred to the acceptor material and extracted at the cathode (metal electrode). Holes travel through the donor layer to the anode (transparent electrode). Most of the available donor materials work well only in the visible region, which ultimately affects the device efficiency. It is necessary to harvest the NIR photons to further improve the efficiency of organic solar cells.

In 2011, Wang and co-workers, demonstrated the feasibility of upconversion in P3HT:PCBM organic solar cells.[227] Commercial UC phosphor based on YF_3:Yb,Er with an UC quantum efficiency of 0.19% (excitation density: 250 mW cm^{-2}) was used us UC source and they obtained a photocurrent density of ca. 16.5 µA cm^{-2} under a laser illumination intensity of ca. 25 mW cm^{-2}. Later in 2012, the same group reported the application of dual functional upconverting Yb,Er-doped MoO_3 film in P3HT:PCBM solar cells.[228] The MoO_3 matrix act as a hole extraction layer while the Yb^{3+} sensitized Er^{3+} dopants upconvert the NIR photons. The authors found that the upconversion contribution to the short-circuit current was less than 1% under one-sun (AM1.5 G) illumination. Wu *et al.* applied $NaYF_4$:Yb,Er upconversion nanoparticles on the rear side of P3HT:PCBM solar cells and studied their effect on device performance under 980 nm laser illumination. The UC layer was fabricated by spray coating a thick layer of UC nanoparticles from a hexane solution on the back side of the ITO glass substrate. They observed an enhancement of 5 µA in the short-circuit current and maximum output power of 9.05 µW with 980 nm laser. However, illumination with simulated solar irradiation (AM 1.5G), the UC effects did not improve the device

efficiency. The photocurrent of device decreased significantly due to the scattering of incoming photons by $NaYF_4$:Yb,Er film.[229]

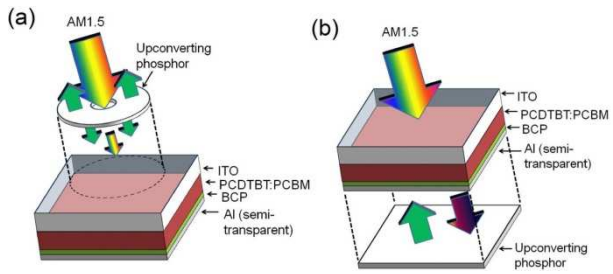

Fig. 18 Schematic of the organic photovoltaic device with an upconversion phosphor placed (a) in front and (b) behind the device. Reprinted with permission from Ref 230. Copyright 2012, American Institute of Physics.

Adikaari et al. demonstrated the application of Y_2BaZnO_5:Yb,Ho upconversion phosphors to PCDTBT:PCBM (PCDTBT:poly[N-9'-heptadecanyl-2,7-carbazole-alt-5,5(4',7'-di-2-thienyl-2',1',3' benzothiadiazole]) organic solar cells in order to utilize the NIR solar spectrum.[230] The authors presented two different device configuration for the use of an UC phosphor with OPV devices. The UC phosphors were made as pellets using a press and placed as shown in Fig. 18. In the first configuration, the UC phosphor was placed in front of the device, while in the second configuration, the phosphor was placed on the rear side of the device. The PCDTBT:PCBM active layer mainly absorbs the visible photons, whereas Y_2BaZnO_5:Yb,Ho phosphors absorb in the NIR region of 870–1030 nm due to the $^2F_{7/2}$ - $^2F_{5/2}$ (Yb^{3+}) transition. More importantly, the UC emission peak of the phosphor well matches with the absorption peak of the PCDTBT:PCBM active layer. They showed that when upconversion phosphors placed behind the device, a maximum photocurrent density of 16 μA cm^{-2} can be achieved when illuminated with a 986 nm laser (excitation density: ~390 mW cm-2). Recently, Guo and co-workers, doped $NaYF_4$:Yb,Er nanocomposites into PCDTBT:PCBM blend as a bifunctional additive to improve performance of inverted polymer BHJ solar cells. The doped UC nanocomposites exhibited both the NIR light harvesting as well as light scattering properties, which enhanced the device performance. With optimized device fabrication, the PCE of 6.87% was obtained, which is 19.1% higher than that of device without upconversion nanocomposites.[231]

6. Conclusions and perspectives

In this review, we have presented the advancements in synthesis and solar cell applications of upconversion nanomaterials. One of the major challenge affecting the solar cell efficiencies is the spectral mismatch between the incident solar spectrum and the semiconductor. Most of the sub-bandgap photons are not absorbed by the semiconductors and are transmitted. This decreases the cell efficiency to larger extend. Spectral converters such as upconversion nanomaterials which can convert the NIR light into visible light, have shown promising application to reduce the transparency losses in large bandgap semiconductor solar cells. However, there are major drawbacks associated with upconversion materials limits the practical application of upconverters for solar cells. First, the efficiency of upconversion nanomaterials used for solar cells is very low and needs to be improved. Different methods are available to improve the UC efficiency such as, impurity doping, use of plasmonic structures and construction of core-shell UC nanomaterials, have been discussed in this review. Impurity doping strategy has exhibited great potential as simple and efficient method to improve UC emission. Second, only very small fraction of sub-bandgap sunlight can be upconverted due to the narrow absorption cross-section of Ln^{3+} ions. Broadening the absorption spectrum is another area needs more attention. There are only few works have been done in this area. Broadening the absorption spectrum for lanthanide upconverters can be achieved by employing external sensitizers such as quantum dots[232] or organic dyes.[233] These sensitizers can absorb over a broad range and emit in the lanthanides absorption region. Pan *et al.* proved the viability of this method in c-Si solar cells by placing PbS QDs below the upconverter layer. They have experimentally proved that the combination of Yb, Er doped phosphor with QDs enhances the upconversion and the increased upconverted emission resulted in higher currents in the solar cell. Another approach to broaden the absorption spectrum is to use Nd^{3+} as a second-sensitizer to sensitize the first sensitizer Yb^{3+}.[234,235] Nd^{3+} has multiple NIR excitation bands at wavelengths shorter than 980 nm, such as 730, 808, and 865 nm which favours the broadband absorption. With large absorption cross-section Nd^{3+} can absorb shorter wavelength lights effectively and transfer its energy to Yb^{3+}. Investigation on these issues is still in the initial stage and the application to solar cells is comparatively less. Despite the good progress, there are many exciting areas available for researchers to explore the practical application of upconversion nanomaterials as spectral converters for solar cells.

Acknowledgements

This work was supported by the Priority Research Center Program (2013-055999) and Basic Science Research Program (2012R1A1A2043731) through the National Research Foundation of Korea (NRF).

Notes and References

Department of Chemistry and GETRC, Kongju National University, 182, Shinkwondong, Kongju, 314-701, Chungnam-do, Republic of Korea. Phone:+82-41-850-8496; Fax: +82-41-850-8613; E-mail: jkim@kongju.ac.kr

1 A. J. Nozik and J. Miller, *Chem. Rev*., 2010, **110**, 6443-6445.
2 K. Kalyanasundaram and M. Gratzel, *J. Mater. Chem*., 2012, **22**, 24190-24194.
3 H. Aguas, S. K. Ram, A. Araujo, D. Gaspar, A. Vicente, S. A. Filonovich, E. Fortunato, R. Martins and I. Ferreira, *Energy Environ. Sci*., 2011, **4**, 4620-4632.
4 G. Conibeer, *Mater. Today*, 2007, **10**, 42-50

5 D. M. Powell, M. T. Winkler, H. J. Choi, C. B. Simmons, D. B. Needleman and T. Buonassisi, *Energy Environ. Sci*., 2012, **5**, 5874-5883.

6 R. D. Costa, F. Lodermeyer, R. Casillas and D. M. Guldi, *Energy Environ. Sci*., 2014, **7**, 1281-1296.

7 W. Shockley and H. J. Queisser, *J. Appl. Phys*., 1961, **32**, 510-519.

8 B. O'Regan and M. Gratzel, *Nature*, 1991, **353**, 737-740.

9 M. Law, L. E. Greene, J. C. Johnson, R. Saykally and P. D. Yang, *Nat. Mater*., 2005, 4, 455-459

10 E. H. Sargent, *Nat. Photonics*, 2012, **6**, 133-135.

11 G. Li, V. Shrotriya, J. S. Huang, Y. Yao, T. Moriarty, K. Emery and Y. Yang, *Nat. Mater*., 2005, **4**, 864-868.

12 P.-L. T. Boudreault, A. Najari and M. Leclerc, *Chem. Mater*., 2010, **23**, 456-469.

13 T. Todorov and D. B. Mitzi, *Eur. J. Inorg. Chem*., 2010, 17-28

14 B. S. Richards, *Sol. Energy Mater. Sol. Cells*, 2006, **90**, 2329-2337.

15 M. S. Leite, R. L. Woo, J. N. Munday, W. D. Hong, S. Mesropian, D. C. Law and H. A. Atwater, *Appl. Phys. Lett*., 2013, **102**, 033901.

16 K. X. Wang, Z. Yu, V. Liu, Y. Cui, and S. Fan, *Nano Lett*., 2012, **12**, 1616-1619.

17 J. Grandidier, D. M. Callahan, J. N. Munday, and H. A. Atwater, *Adv. Mater*., 2011, **23**, 1272-1276.

18 R. J. Veenkamp and W. N Ye, *J. Appl. Phys*., 2014, **115**, 124317.

19 Q. Y. Zhang and X. Y. Huang, *Prog. Mater. Sci*., 2010, **55**, 353-427.

20 T. Trupke, M. A. Green and P. Wurfel, *J. Appl. Phys*., 2002, **92**, 4117-4122.

21 F. Auzel, *Chem. Rev.*, 2003, **104**, 139-174.

22 G. Blasse and B. C. Grabmaier, Luminescent Materials, Springer, Berlin, 1994.

23 T. N. Singh-Rachford and F. N. Castellano, *Coord. Chem. Rev*., 2010, **254**, 2560-2573.

24 J. S. Chivian, W. E. Case and D. D. Eden, *Appl. Phys. Lett*., 1979, **35**, 124.

25 G. H. Dieke, Spectra and Energy Levels of Rare Earth Ions in Crystals, Wiley, New York, 1968.

26 F. Wang and X. Liu, *Chem. Soc. Rev.*, 2009, **38**, 976-989.

27 J. Ohwaki and Y. Wang, *Jpn. J. Appl. Phys*., 1994, **33**, L334-L337.

28 F. Auzel, D. Pecile and D. Morin, *J. Electrochem. Soc*., 1975, **122**, 101-107.

29 P. P. Fedorov, A. A. Luginina, S. V. Kuznetsov and V. V. Osiko, *J. Fluorine Chem*., 2011, **132**, 1012-1039.

30 F. Vetrone and J. A. Capobianco, *Int. J. Nanotechnol*., 2008, **5**, 1306-1339.

31 Y.-W. Zhang, X. Sun, R. Si, L.-P. You and C.-H. Yan, *J. Am. Chem. Soc*., 2005, **127**, 3260-3261.

32 J.-C. Boyer, F. Vetrone, L. A. Cuccia and J. A. Capobianco, *J. Am. Chem. Soc*, 2006, **128**, 7444-7445.

33 J.-C. Boyer, L. A. Cuccia and J. A. Capobianco, *Nano Lett*., 2007, **7**, 847-852.

34 H.-X. Mai, Y.-W. Zhang, L.-D. Sun and C.-H. Yan, *J. Phys. Chem. C*, 2007, **111**, 13730-13739.

35 H.-X. Mai, Y.-W. Zhang, R. Si, Z.-G. Yan, L.-d. Sun, L.-P. You and C.-H. Yan, *J. Am. Chem. Soc*, 2006, **128**, 6426-6436.

36 Y.-P. Du, Y.-W. Zhang, L.-D. Sun and C.-H. Yan, *Dalton Trans*., 2009, 8574-8581.

37 X. Ye, J. E. Collins, Y. Kang, J. Chen, D. T. N. Chen, A. G. Yodh and C. B. Murray, *Proc. Natl. Acad. Sci. U. S. A.*, 2010, **107**, 22430-22435.

38 G. S. Yi and G. M. Chow, *Adv. Funct. Mater*., 2006, **16**, 2324-2329.

39 J. Shan, X. Qin, N. Yao, and Y. Ju, *Nanotechnology*, 2007, 18, 445607.

40 W. Kong, R. Wei, N. Yao and Y. Ju, *J. Appl. Phys*., 2010, **107**, 054901.

41 J. Shan and Y. Ju, *Appl. Phys. Lett*., 2007, **91**, 123103.

42 Y. Wei, F. Lu, X. Zhang and D. Chen, *Chem. Mater*., 2006, **18**, 5733-5737.

43 C. Liu, H. Wang, X. Zhang and D. Chen, *J. Mater. Chem*., 2009, **19**, 489-496.

44 C. Liu, H. Wang, X. Li and D. Chen, *J. Mater. Chem*., 2009, **19**, 3546-3553.

45 H. Na, K. Woo, K. Lim and H. S. Jang, *Nanoscale*, 2013, **5**, 4242-4251.

46 X. Li, S. Gai, C. Li, D. Wang, N. Niu, F. He and P. Yang, *Inorg. Chem*., 2012, **51**, 3963-3971.

47 G. K. Das and T. T. Y. Tan, *J. Phys. Chem. C,*, 2008, **112**, 11211-11217.

48 G. K. Das, B. C. Heng, S.-C. Ng, T. White, J. S. C. Loo, L. D'Silva, P. Padmanabhan, K. K. Bhakoo, S. T. Selvan and T. T. Y. Tan, *Langmuir*, 2010, **26**, 8959-8965.

49 T. Paik, T. R. Gordon, A. M. Prantner, H. Yun and C. B. Murray, *ACS Nano*, 2013, **7**, 2850-2859.

50 R. Si, Y.-W. Zhang, H.-P. Zhou, L.-D. Sun and C.-H. Yan, *Chem. Mater*, 2006, **19**, 18-27.

51 R. Si, Y.-W. Zhang, L.-P. You and C.-H. Yan, *Angew. Chem. Int. Ed*., 2005, **44**, 3256-3260.

52 Z. Li, and Y. Zhang, *Nanotechnology,* 2008, 19, 345606.

53 F. Shi, J. Wang, D. Zhang, G. Qin and W. Qin, *J. Mater. Chem*., 2011, **21**, 13413-13421.

54 C. Zhao, X. Kong, X. Liu, L. Tu, F. Wu, Y. Zhang, K. Liu, Q. Zeng and H. Zhang, *Nanoscale*, 2013, **5**, 8084-8089.

55 J. Zhao, Z. Lu, Y. Yin, C. McRae, J. A. Piper, J. M. Dawes, D. Jin and E. M. Goldys, *Nanoscale*, 2013, **5**, 944-952.

56 W. Niu, L. T. Su, R. Chen, H. Chen, Y. Wang, A. Palaniappan, H. Sun and A. I. Yoong Tok, *Nanoscale*, 2014, **6**, 817-824.

57 P. Ramasamy, P. Chandra, S. W. Rhee and J. Kim, *Nanoscale*, 2013, **5**, 8711-8717.

58 F. Shi, J. Wang, X. Zhai, D. Zhao and W. Qin, *CrystEngComm*, 2011, **13**, 3782-3787.

59 G. K. Das, N. J. J. Johnson, J. Cramen, B. Blasiak, P. Latta, B. Tomanek and F. C. J. M. van Veggel, *J. Phys. Chem. Lett*., 2012, **3**, 524-529.

60 G. Chen, T. Y. Ohulchanskyy, W. C. Law, H. Agren and P. N. Prasad, *Nanoscale*, 2011, **3**, 2003-2008.

61 C. T. Xu, P. Svenmarker, H. Liu, X. Wu, M. E. Messing, L. R. Wallenberg and S. Andersson-Engels, *ACS Nano*, 2012, **6**, 4788-4795.

62 Q. Zeng, B. Xue, Y. Zhang, D. Wang, X. Liu, L. Tu, H. Zhao, X. Kong and H. Zhang, *CrystEngComm*, 2013, **15**, 4765-4772.

63 R. Deng, X. Xie, M. Vendrell, Y.-T. Chang and X. Liu, *J. Am. Chem. Soc*, 2011, **133**, 20168-20171.

64 G. Jiang, J. Pichaandi, N. J. J. Johnson, R. D. Burke and F. C. J. M. van Veggel, *Langmuir*, 2012, **28**, 3239-3247.

65 W. Ren, G. Tian, S. Jian, Z. Gu, L. Zhou, L. Yan, S. Jin, W. Yin and Y. Zhao, *RSC Adv*., 2012, **2**, 7037-7041.

66 F. Wang, J. Wang and X. Liu, *Angew. Chem. Int. Ed*., 2010, **49**, 7456-7460.

67 H. Schäfer, P. Ptacek, O. Zerzouf and M. Haase, *Adv. Funct. Mater*., 2008, **18**, 2913-2918.

68 H.-T. Wong, F. Vetrone, R. Naccache, H. L. W. Chan, J. Hao and J. A. Capobianco, *J. Mater. Chem*., 2011, **21**, 16589-16596.

69 F. Zhang, R. Che, X. Li, C. Yao, J. Yang, D. Shen, P. Hu, W. Li and D. Zhao, *Nano Lett.*, 2012, **12**, 2852-2858.

70 Y. I. Park, H. M. Kim, J. H. Kim, K. C. Moon, B. Yoo, K T. Lee, N. Lee, Y. Choi, W. Park, D. Ling, K. Na, W. K. Moon, S. H. Choi, H. S. Park, S.-Y. Yoon, Y. D. Suh, S. H. Lee and T. Hyeon, *Adv. Mater.*, 2012, **24**, 5755-5761.

71 F. Chen, W. Bu, S. Zhang, J. Liu, W. Fan, L. Zhou, W. Peng and J. Shi, *Adv. Funct. Mater*, 2013, **23**, 298-307.

72 H.-S. Qian and Y. Zhang, *Langmuir*, 2008, **24**, 12123-12125.

73 J. Pichaandi, J.-C. Boyer, K. R. Delaney and F. C. J. M. van Veggel, *J. Phys. Chem. C*, 2011, **115**, 19054-19064.

74 M. Banski, A. Podhorodecki and J. Misiewicz, *Phys. Chem. Chem. Phys*., 2013, **15**, 19232-19241.

75 A. A. Arnold, V. Terskikh, Q. Y. Li, R. Naccache, I. Marcotte and J. A. Capobianco, *J. Phys. Chem. C*, 2013, **117**, 25733-25741.

76 Y. Deng, H. Wang, W. Gu, S. Li, N. Xiao, C. Shao, Q. Xu and L. Ye, *J. Mater. Chem. B*, 2014, **2**, 1521-1529.

77 N. J. J. Johnson, W. Oakden, G. J. Stanisz, R. Scott Prosser and F. C. J. M. van Veggel, *Chem. Mater.*, 2011, **23**, 3714-3722.

78 H. Xing, S. Zhang, W. Bu, X. Zheng, L. Wang, Q. Xiao, D. Ni, J. Zhang, L. Zhou, W. Peng, K. Zhao, Y. Hua and J. Shi, *Adv. Mater*., 2014, DOI: 10.1002/adma.201305222.

79 G. Chen, J. Shen, T. Y. Ohulchanskyy, N. J. Patel, A. Kutikov, Z. Li, J. Song, R. K. Pandey, H. Ågren, P. N Prasad and G. Han, *ACS Nano*, 2012, **6**, 8280-8287.

80 X. Teng, Y. Zhu, W. Wei, S. Wang, J. Huang, R. Naccache, W. Hu, A. I. Y. Tok, Y. Han, Q. Zhang, Q. Fan, W. Huang, J. A. Capobianco and L. Huang, *J. Am. Chem. Soc.*, 2012, **134**, 8340-8343.

81 M. Pang, J. Feng, S. Song, Z. Wang and H. Zhang, *CrystEngComm.*, 2013, **15**, 6901-6904.

82 X. Sun, Y.-W. Zhang, Y.-P. Du, Z.-G. Yan, R. Si, L.-P. You and C.-H. Yan, *Chem. Eur. J*., 2007, **13**, 2320-2332.

83 H. Qiu, G. Chen, R. Fan, L. Yang, C. Liu, S. Hao, M. J. Sailor, H. gren, C. Yang and P. N. Prasad, *Nanoscale*, 2014, **6**, 753-757.

84 Y.-P. Du, X. Sun, Y.-W. Zhang, Z.-G. Yan, L.-D. Sun and C.-H. Yan, *Cryst. Growth Des*., 2009, **9**, 2013-2019.

85 D. Chen, Y. Yu, F. Huang, H. Lin, P. Huang, A. Yang, Z. Wang and Y. Wang, *J. Mater. Chem*., 2012, **22**, 2632-2640.

86 D. Chen, Y. Yu, F. Huang, P. Huang, A. Yang, Z. Wang and Y. Wang, *Chem. Commun.*, 2011, **47**, 11083-11085.

87 J. Wang, F. Wang, C. Wang, Z. Liu and X. Liu, *Angew. Chem. Int. Ed*., 2011, **50**, 10369-10372.

88 Y. Zhang, J. D. Lin, V. Vijayaragavan, K. K. Bhakoo and T. T. Y. Tan, *Chem. Commun*., 2012, **48**, 10322-10324.

89 G. Yi, Y. Peng and Z. Gao, *Chem. Mater.*, 2011, **23**, 2729-2734.

90 X. Wang and Y. Li, *Chem. Eur. J.*, 2003, **9**, 5627-5635.

91 X. Wang and Y. Li, *Angew. Chem. Int. Ed*., 2002, **41**, 4790-4793.

92 X. Wang, X. M. Sun, D. Yu, B. S. Zou and Y. Li, *Adv. Mater*., 2003, **15**, 1442-1445.

93 F. Zhang and D. Zhao, *ACS Nano*, 2008, **3**, 159-164.

94 Z. Xu, C. Li, P. Yang, C. Zhang, S. Huang and J. Lin, *Cryst. Growth Des*., 2009, **9**, 4752-4758.

95 X. Wang, J. Zhuang, Q. Peng, Y. Li, *Nature*, 2005, **437,** 121-124.

96 L. Wang and Y. Li, *Nano Lett.*, 2006, **6**, 1645-1649.

97 X. Wang, J. Zhuang, Q. Peng and Y. Li, *Inorg. Chem*., 2006, **45**, 6661-6665.

98 L. Wang and Y. Li, *Chem. Mater.*, 2007, **19**, 727-734.

99 F. Zhang, Y. Wan, T. Yu, F. Zhang, Y. Shi, S. Xie, Y. Li, L. Xu, B. Tu and D. Zhao, *Angew. Chem. Int. Ed*., 2007, **119**, 8122-8125.

100 P. Li, Q. Peng and Y. Li, *Adv. Mater*., 2009, **21**, 1945-1948.

101 G. Wang, Q. Peng and Y. Li, *J. Am. Chem. Soc*, 2009, **131**, 14200-14201.

102 F. Wang, Y. Han, C. S. Lim, Y. H. Lu, J. Wang, J. Xu, H. Chen, C. Zhang, M. Hong and X. Liu, *Nature*, 2010, **463**, 1061-1065.

103 D. Chen, Y. Yu, F. Huang, P. Huang, A. Yang and Y. Wang, *J. Am. Chem. Soc.*, 2010, **132**, 9976-9978.

104 D. Yang, Y. Dai, P. Ma, X. Kang, Z. Cheng, C. Li and J. Lin, *Chem. Eur. J.*, 2013, **19**, 2685-2694.

105 G. Tian, Z. Gu, L. Zhou, W. Yin, X. Liu, L. Yan, S. Jin, W. Ren, G. Xing, S. Li and Y. Zhao, *Adv. Mater*., 2012, **24**, 1226-1231.

106 G. Wang, Q. Peng and Y. Li, *Chem. Commun.*, 2010, **46**, 7528-7529.

107 Z.-j. Liu, X.-x. Song and Q. Tang, *Nanoscale*, 2013, **5**, 5073-5079.

108 Z. Bai, H. Lin, J. Johnson, S. C. Rong Gui, K. Imakita, R. Montazami, M. Fujii and N. Hashemi, *J. Mater. Chem. C*, 2014, **2**, 1736-1741.

109 C. Li, Z. Quan, J. Yang, P. Yang and J. Lin, *Inorg. Chem*., 2007, **46**, 6329-6337.

110 C. Li, J. Yang, P. Yang, X. Zhang, H. Lian and J. Lin, *Cryst. Growth Des*., 2008, **8**, 923-929.

111 C. Li, Z. Quan, P. Yang, J. Yang, H. Lian and J. Lin, *J. Mater. Chem.*, 2008, **18**, 1353-1361.

112 F. He, P. Yang, D. Wang, N. Niu, S. Gai and X. Li, *Inorg. Chem*., 2011, **50**, 4116-4124.

113 J. H. Zeng, J. Su, Z. H. Li, R. X. Yan and Y. D. Li, *Adv. Mater*., 2005, **17**, 2119-2123.

114 H. Qiu, G. Chen, L. Sun, S. Hao, G. Han and C. Yang, *J. Mater. Chem*., 2011, **21**, 17202-17208.

115 H. Chen, X. Zhai, D. Li, L.Wang, D. Zhao, and W. Qin, *J. Alloys. Compd.,* 2012, **511,** 70-73.

116 P. Qiu, N. Zhou, Y. Wang, C. Zhang, Q. Wang, R. Sun, G. Gao and D. Cui, *CrystEngComm.*, 2014, **16**, 1859-1863.

117 F.Wang, D. K. Chatterjee, Z. Li, Y. Zhang, X. Fan and M. Wang, *Nanotechnology,* 2006, **17,** 5786-5791.

118 F. Wang and X. Liu, *J. Am. Chem. Soc.*, 2008, **130**, 5642-5643.

119 F. Vetrone, R. Naccache, A. Juarranz de la Fuente, F. Sanz-Rodriguez, A. Blazquez-Castro, E. M. Rodriguez, D. Jaque, J. G. Sole and J. A. Capobianco, *Nanoscale*, 2010, **2**, 495-498.

120 G. Tian, L. Duan, X. Zhang, W. Yin, L. Yan, L. Zhou, X. Liu, X. Zheng, J. Li, Z. Gu and Y. Zhao, *Chem. Asian J*., 2014, DOI: 10.1002/asia.201301695.

121 Z. Wang, C. Liu, L. Chang and Z. Li, *J. Mater. Chem*., 2012, **22**, 12186-12192.

122 F. Zhang, J. Li, J. Shan, L. Xu and D. Zhao, *Chem. Eur. J.*, 2009, **15**, 11010-11019.

123 H.-T. Wong, M.-K. Tsang, C.-F. Chan, K.-L. Wong, B. Fei and J. Hao, *Nanoscale*, 2013, **5**, 3465-3473.

124 S. Wu, N. Duan, X. Ma, Y. Xia, H. Wang, Z. Wang and Q. Zhang, *Anal. Chem.*, 2012, **84**, 6263-6270.

125 H. Liu, W. Lu, H. Wang, L. Rao, Z. Yi, S. Zeng and J. Hao, *Nanoscale*, 2013, **5**, 6023-6029.

126 Q. Zhao, B. Shao, W. Lü, Y. Jia, W. Lv, M. Jiao and H. You, *Cryst. Growth Des*., 2014, **14**, 1819-1826.

127 B.-L. An, L.-H. Ma, J.-H. Fang, Y.-Q. Wang and J.-Q. Xu, *RSC Adv.*, 2013, **3**, 19909-19912.

128 L. Guo, Y. Wang, Z. Zou, B. Wang, X. Guo, L. Han and W. Zeng, *J. Mater. Chem. C*, 2014, **2**, 2765-2772.

129 S. Gong, Z. Ren, S. Jiang, M. Li, X. Li, X. Wei, G. Xu, G. Shen and G. Han, *The J. Phys. Chem. C*, 2014, **118**, 5486-5493.

130 W. Yin, L. Zhao, L. Zhou , Z. Gu, X. Liu, G. Tian , S. Jin , L. Yan, W. Ren, G. Xing and Y. Zhao *Chem. Eur. J*., 2012, **18**, 9239-9245.

131 W. Yin, L. Zhou, Z. Gu, G. Tian, S. Jin, L. Yan, X. Liu, G. Xing, W. Ren, F. Liu, Z. Pan and Y. Zhao, *J. Mater. Chem*., 2012, **22**, 6974-6981.

132 L. Zhou, Z. Gu, X. Liu, W. Yin, G. Tian, L. Yan, S. Jin, W. Ren, G. Xing, W. Li, X. Chang, Z. Hu and Y. Zhao, *J. Mater. Chem*., 2012, **22**, 966-974.

133 G. Li, M. Shang, D. Geng, D. Yang, C. Peng, Z. Cheng and J. Lin, *CrystEngComm.*, 2012, **14**, 2100-2111.

134 Y. Song, Y. Huang, L. Zhang, Y. Zheng, N. Guo and H. You, *RSC Adv*., 2012, **2**, 4777-4781.

135 J. W. Stouwdam and F. C. J. M. van Veggel, *Nano Lett.*, 2002, **2**, 733-737.

136 G. Yi, H. Lu, S. Zhao, Y. Ge, W. Yang, D. Chen and L.-H. Guo, *Nano Lett.*, 2004, **4**, 2191-2196.

137 F. He, N. Niu, L. Wang, J. Xu, Y. Wang, G. Yang, S. Gai and P. Yang, *Dalton Trans.*, 2013, **42**, 10019-10028.

138 G.-S. Yi and G.-M. Chow, *J. Mater. Chem*., 2005, **15**, 4460-4464.

139 K. Zheng, W. Song, C. Lv, Z. Liu and W. Qin, *CrystEngComm.*, 2014, **DOI:** 10.1039/C4CE00036F.

140 Q. Lu, Y. Hou, A. Tang, Y. Lu, L. Lv and F. Teng, *J. Appl. Phys.*, 2014, **115**, 074309-074304.

141 H. J. Kitchen, S. R. Vallance, J. L. Kennedy, N. Tapia-Ruiz, L. Carassiti, A. Harrison, A. G. Whittaker, T. D. Drysdale, S. W. Kingman and D. H. Gregory, *Chem. Rev.*, 2013, **114**, 1170-1206.

142 H.-Q. Wang and T. Nann, *ACS Nano*, 2009, **3**, 3804-3808.

143 C. Mi, Z. Tian, C. Cao, Z. Wang, C. Mao and S. Xu, *Langmuir*, 2011, **27**, 14632-14637.

144 N. Niu, F. He, S. Gai, C. Li, X. Zhang, S. Huang and P. Yang, *J. Mater. Chem*., 2012, **22**, 21613-21623.

145 F. Li, C. Li, X. Liu, Y. Chen, T. Bai, L. Wang, Z. Shi and S. Feng, *Chem. Eur. J*., 2012, **18**, 11641-11646.

146 S. Pan, R. Deng, J. Feng, S. Song, S. Wang, M. Zhu and H. Zhang, *CrystEngComm.*, 2013, **15**, 7640-7643.

147 E. R. Parnham and R. E. Morris, *Acc. Chem. Res.*, 2007, **40**, 1005-1013.

148 V. I. Pârvulescu and C. Hardacre, *Chem. Rev.*, 2007, **107**, 2615-2665.

149 X. Liu, J. Zhao, Y. Sun, K. Song, Y. Yu, C. Du, X. Kong and H. Zhang, *Chem. Commun.*, 2009, 6628-6630.

150 C. Chen, L.-D. Sun, Z.-X. Li, L.-L. Li, J. Zhang, Y.-W. Zhang and C.-H. Yan, *Langmuir*, 2010, **26**, 8797-8803.

151 G. Glaspell, J. Anderson, J. R. Wilkins and M. S. El-Shall, *J. Phys. Chem. C*, 2008, **112**, 11527-11531.

152 X. Qin, T. Yokomori and Y. Ju, *Appl. Phys. Lett.*, 2007, **90**, 073104.

153 W. Kong, J. Shan, and Y. Ju, *Mater. Lett*., 2010, **64**, 688-691.

154 F. Wang, R. Deng, and X. Liu, *Nat. Protoc*., 2014, **9**, 1634-1644.

155 R. H. Page, K. I. Schaffers, P. A. Waide, J. B. Tassano, S. A. Payne, W. F. Krupke and W. K. Bischel, *J. Opt. Soc. Am. B* 1998, **15**, 996-1008.

156 J.-C. Boyer and F. C. J. M. van Veggel, *Nanoscale*, 2010, **2**, 1417-1419.

157 D. Chen and Y. Wang, *Nanoscale*, 2013, **5**, 4621-4637.

158 G. Y. Chen, H. C. Liu, G. Somesfalean, Y. Q. Sheng, H. J. Liang, Z. G. Zhang, Q. Sun and F. P. Wang, *Appl. Phys. Lett.*, 2008, **92**, 113114.

159 G. Chen, H. Liu, H. Liang, G. Somesfalean and Z. Zhang, *J. Phys. Chem. C*, 2008, **112**, 12030-12036.

160 V. Mahalingam, R. Naccache, F. Vetrone and J. A. Capobianco, *Opt. Express*, 2012, **20**, 111-119.

161 Q. Cheng, J. Sui and W. Cai, *Nanoscale*, 2012, **4**, 779-784.

162 D. Yang, Y. Dai, P. a. Ma, X. Kang, M. Shang, Z. Cheng, C. Li and J. Lin, *J. Mater. Chem*., 2012, **22**, 20618-20625.

163 Q. Dou and Y. Zhang, *Langmuir*, 2011, **27**, 13236-13241.

164 Q. Huang, J. Yu, E. Ma and K. Lin, *J. Phys. Chem. C*, 2010, **114**, 4719-4724.

165 L. Lei, D. Chen, P. Huang, J. Xu, R. Zhang and Y. Wang, *Nanoscale*, 2013, **5**, 11298-11305.

166 H. Zhang, D. Xu, Y. Huang and X. Duan, *Chem. Commun.*, 2011, **47**, 979-981.

167 W. Xu, S. Xu, Y. Zhu, T. Liu, X. Bai, B. Dong, L. Xu and H. Song, *Nanoscale*, 2012, **4**, 6971-6973.

168 M. Saboktakin, X. Ye, S. J. Oh, S.-H. Hong, A. T. Fafarman, U. K. Chettiar, N. Engheta, C. B. Murray and C. R. Kagan, *ACS Nano*, 2012, **6**, 8758-8766.

169 W. Zhang, F. Ding and S. Y. Chou, *Adv. Mater.*, 2012, **24**, OP236-OP241.

170 M. Saboktakin, X. Ye, U. K. Chettiar, N. Engheta, C. B. Murray and C. R. Kagan, *ACS Nano*, 2013, **7**, 7186-7192.

171 Q.-C. Sun, H. Mundoor, J. C. Ribot, V. Singh, I. I. Smalyukh and P. Nagpal, *Nano Lett.*, 2013, **14**, 101-106.

172 H. Zhang, Y. Li, I. A. Ivanov, Y. Qu, Y. Huang and X. Duan, *Angew. Chem. Int. Ed*., 2010, **49**, 2865-2868.

173 Z. Q. Li, S. Chen, J. J. Li, Q. Q. Liu, Z. Sun, Z. B. Wang and S. M. Huang, *J. Appl. Phys.*, 2012, **111**, 014310.

174 P. Yuan, Y. H. Lee, M. K. Gnanasammandhan, Z. Guan, Y. Zhang and Q.-H. Xu, *Nanoscale*, 2012, **4**, 5132-5137.

175 Z. Li, L. Wang, Z. Wang, X. Liu and Y. Xiong, *J. Phys. Chem. C*, 2011, **115**, 3291-3296.

176 F. Zhang, G. B. Braun, Y. Shi, Y. Zhang, X. Sun, N. O. Reich, D. Zhao and G. Stucky, *J. Am. Chem. Soc.,* 2010, **132**, 2850-2851.

177 G.-S. Yi and G.-M. Chow, *Chem. Mater.*, 2006, **19**, 341-343.

178 Y.-F. Wang, L.-D. Sun, J.-W. Xiao, W. Feng, J.-C. Zhou, J. Shen and C.-H. Yan, *Chem. A. Eur. J.*, 2012, **18**, 5558-5564.

179 F. Vetrone, R. Naccache, V. Mahalingam, C. G. Morgan and J. A. Capobianco, *Adv. Funct. Mater.*, 2009, **19**, 2924-2929.

180 F. Wang, R. Deng, J. Wang, Q. Wang, Y. Han, H. Zhu, X. Chen and X. Liu, *Nat. Mater.* 2011, **10**, 968-973.

181 P. Gibart, F. Auzel, J. C. Guillaume and K. Zahraman, *Jpn. J. Appl. Phys.,* Part 1, 1996, **35,** 4401-4402.

182 A. Shalav, B. S. Richards, T. Trupke, K. W. Krämer and H. U. Güdel, *Appl. Phys. Lett.*, 2005, **86**, 013505.

183 S. Fischer, J. C. Goldschmidt, P. Löper, G. H. Bauer, R. Brüggemann, K. Krämer, D. Biner, M. Hermle and S. W. Glunz, *J. Appl. Phys.*, 2010, **108**, 044912.

184 S. Ivanova, F. Pelle, A. Tkachuk, M. F. Joubert, Y Guyot and V. P. Gapontzev, *J. Lumin.,* 2008, **128,** 914-917.

185 X. F. Liang, X. Y. Huang and Q. Y. Zhang, *J. Fluoresc*., 2009, **19**, 285-289.

186 F. Xin, S. Zhao, L. Huang, D. Deng, G. Jia, H. Wang and S. Xu., *Mater. Lett.,* 2012, **78,** 75-77.

187 X. F. Wang, X. H. Yan and C. X. Kan, *J. Mater. Chem.,* 2011, **21,** 4251-4256.

188 R. Martín-Rodríguez, S. Fischer, A. Ivaturi, B. Froehlich, K. W. Krämer, J. C. Goldschmidt, B. S. Richards and A. Meijerink, *Chem.Mater.*, 2013, **25**, 1912-1921.

189 S. Ivanova and F. Pelle, *J. Opt. Soc. Am. B,* 2009, **26,** 1930-1938.

190 A. Boccolini, R. Faoro, E. Favilla, S. Veronesi and M. Tonelli, *J. Appl. Phys.*, 2013, **114**, 064904.

191 Y. Qian, R. Wang, B. Wang, B. Zhang and S. Gao, *RSC Adv.*, 2014, **4**, 6652-6656.

192 F. Lahoz, *Opt. Lett*., 2008, **33,** 2982-2984.

193 F. Lahoz, C. Perez-Rodriguez, S. E. Hernandez, I. R. Martin, V. Lavin and U. R. Rodriguez-Mendoza, *Sol. Energy Mater. Sol. Cells*, 2011, **95,** 1671-1677.

194 D. Q. Chen, L. Lei, A. P. Yang, Z. X. Wang and Y. S. Wang, *Chem. Commun.,* 2012, **48,** 5898-5900.

195 X. D. Zhang, X. Jin, D. F. Wang, S. Z. Xiong, X. H. Geng and Y. Zhao, *Phys. Status Solidi. C,* 2010, **7,** 1128-1131.

196 J. de Wild, A. Meijerink, J. K. Rath, W. G. J. H. M. van Sark and R. E. I. Schropp, *Sol. Energy Mater. Sol. Cells,* 2010, **94,** 1919-1922.

197 J. de Wild, J. K. Rath, A. Meijerink, W. G. J. H. M. van Sark and R. E. I. Schropp, *Sol. Energy Mater. Sol. Cells,* 2010, **94,** 2395-2398.

198 Z. Q. Li, X. D. Li, Q. Q. Liu, X. H. Chen, Z. Sun, C. Liu, X. J. Ye and S. M. Huang, *Nanotechnology,* 2012, **23,** 025402.

199 S. L. Zhao, S. Q. Xu, G. H. Jia, D. G. Deng, L. H. Huang and H. P. Wang, *Mater. Lett.,* 2011, **65,** 2407-2409.

200 Y. Chen, W. He, Y. Jiao, H. Wang, X. Hao, J. Lu and S. Yang, *J. Lumin.,* 2012, **132,** 2247-2250.

201 J. de Wild, T. F. Duindam, J. K. Rath, A. Meijerink, W. G. J. H. M. van Sark and R. E. I. Schropp, *IEEE J. Photovolt.*, 2013, **3**, 17-21.

202 S. Mathew, A. Yella, P. Gao, R. H. Baker, B. F. E. Curchod, N. A. Astani, I. Tavernelli, U. Rothlisberger, Md. K. Nazeeruddin and Michael Gratzel, *Nat. Photonics*, 2014, **6**, 242-247.

203 T. W. Hamann, R. A. Jensen, A. B. F. Martinson, H. Van Ryswyk and J. T. Hupp, *Energy Environ. Sci*., 2008, **1**, 66-78.

204 K. Lee, S. W. Park, M. J. Ko, K. Kim and N. G. Park, *Nat. Mater*., 2009, **8**, 665-671.

205 G.-B. Shan and G. P. Demopoulos, *Adv. Mater.*, 2010, **22**, 4373-4377.

206 J. Wu, J. Wang, J. Lin, Z. Lan, Q. Tang, M. Huang, Y. Huang, L. Fan, Q. Li and Z. Tang, *Adv. Energy Mater.*, 2012, **2**, 78-81.

207 J. Chang, Y. Ning, S. Wu, W. Niu and S. Zhang, *Adv. Funct. Mater.*, 2013, **23**, 5910-5915.

208 A. Khan, R. Yadav, P. K. Mukhopadhya, S. Singh, C. Dwivedi, V. Dutta and S. Chawla, *J. Nanopart. Res.*, 2011, **13**, 6837-6846.

209 C. Yuan, G. Chen, P. N. Prasad, T. Y. Ohulchanskyy, Z. Ning, H. Tian, L. Sun and H. Agren, *J. Mater. Chem.*, 2012, **22**, 16709-16713.

210 Y. Li, G. Wang, K. Pan, B. Jiang, C. Tian, W. Zhou and H. Fu, *J. Mater. Chem.*, 2012, **22**, 20381-20386.

211 L. Zhang, Q. Tian, W. Xu, X. Kuang, J. Hu, M. Zhu, J. Liu and Z. Chen, *J. Mater. Chem.*, 2012, **22**, 18156-18163.

212 G.-B. Shan, H. Assaaoudi and G. P. Demopoulos, *ACS Appl. Mater. Inter.*, 2011, **3**, 3239-3243.

213 Y. Li, K. Pan, G. Wang, B. Jiang, C. Tian, W. Zhou, Y. Qu, S. Liu, L. Feng and H. Fu, *Dalton Trans.*, 2013, **42**, 7971-7979.

214 J. Zhang, H. Shen, W. Guo, S. Wang, C. Zhu, F. Xue, J. Hou, H. Su, Z. Yuan, *J. Power Sour.,* 2013, **226,** 47-53.

215 L. Liang, Y. Liu and X.-Z. Zhao, *Chem. Commun.*, 2013, **49**, 3958-3960.

216 L. Liang, Y. Liu, C. Bu, K. Guo, W. Sun, N. Huang, T. Peng, B. Sebo, M. Pan, W. Liu, S. Guo and X.-Z. Zhao, *Adv.Mater.*, 2013, **25**, 2174-2180.

217 Z. Zhou, J. Wang, F. Nan, C. Bu, Z. Yu, W. Liu, S. Guo, H. Hu and X.-Z. Zhao, *Nanoscale*, 2014, **6**, 2052-2055.

218 P. Ramasamy and J. Kim, *Chem. Commun.*, 2014, **50**, 879-881.

219 Z. Chen, L. Zhang, Y. Sun, J. Hu and D. Wang, *Adv. Funct. Mater.*, 2009, **19**, 3815-3820.

220 X-H. Lu, Y-Z. Zheng, S-Q. Bi, J-X. Zhao, X. Tao and J-F. Chen, *J. Power Sour.,* 2013, **243,** 588-593.

221 M. J. Lim, Y. N. Ko, Y. C. Kang and K. Y. Jung, *RSC Adv.,* 2014, **4**, 10039-10042.

222 M. Liu, Y. Lu, Z. B. Xie, G. M. Chow, *Sol. Energy Mater. Sol. Cells,* 2011, **95,** 800-803.

223 X. Wu, G. Q. Lu and L. Wang, *Adv. Energy Mater.*, 2013, **3**, 704-707.

224 G. Xie, J. Lin, J. Wu, Z. Lan, Q. Li, Y. Xiao, G. Yue, H. Yue and M. Huang, *Chin. Sci. Bull.*, 2011, **56**, 96-101.

225 L. Li, Y. Yang, M. Zhou, R. Fan, L. L. Qiu, X. Wang, L. Zhang, X. Zhou and J. He, *J. Solid State Chem.,* 2013, **198,** 459-465.

226 Q. Li, J. Lin, J. Wu, Z. Lan, Y. Wang, F. Peng and M. Huang, *Electrochim. Acta,* 2011, **56,** 4980-4984.

227 H.-Q. Wang, M. Batentschuk, A. Osvet, L. Pinna and C. J. Brabec, *Adv.Mater.*, 2011, **23**, 2675-2680.

228 H.-Q. Wang, T. Stubhan, A. Osvet, I. Litzov and C. J. Brabec, *Sol. Energy Mater. Sol. Cells,* 2012, **105,** 196-201.

229 J.-L. Wu, F.-C. Chen, S.-H. Chang, K.-S. Tan and H.-Y. Tuan, *Org. Electron.,* 2012, **13,** 2104-2108.

230 A. A. D. Adikaari, I. Etchart, P.-H. Guéring, M. Bérard, S. R. P. Silva, A. K. Cheetham and R. J. Curry, *J. Appl. Phys.*, 2012, **111**, 094502.

231 W. Guo, K. Zheng,W. Xie, L. Sun, L. Shen, C. Liu, Y. He, Z. Zhang, *Sol. Energy Mater. Sol. Cells,* 2014, **124,** 126-132.

232 A. C. Pan, C. del Canizo, E. Canavos, N. M. Santos, J. P. Leitao and A. Luque, *Sol. Energy Mater. Sol. Cells*, 2010, **94**, 1923-1926.

233 W. Zou, C. Visser, J. A. Maduro, M. S. Pshenichnikov and J. C. Hummelen, *Nat. Photonics*, 2012, **6**, 560-564.

234 X. Xie, N. Gao, R. Deng, Q. Sun, Q.-H. Xu and X. Liu, *J. Am. Chem. Soc*., 2013, **135**, 12608-12611.

235 Y.-F. Wang, G.-Y. Liu, L.-D. Sun, J.-W. Xiao, J.-C. Zhou and C.-H. Yan, *ACS Nano*, 2013, **7**, 7200-7206.